1

2

3 **Propagation of neuronal micronuclei regulates microglial states**

4

5 Sarasa Yano[1], Natsu Asami[2], Yusuke Kishi[8,10], Hikari Kubotani[2], Yuki Hattori[11], Ayako

6 Kitazawa[12,13], Kanehiro Hayashi[12], Ken-ichiro Kubo[12,13], Mai Saeki[8,10], Chihiro Maeda[2], Kaito

7 Akiyama[3], Tomomi Okajima-Takahashi[1], Ban Sato[4,16], Yukiko Gotoh[8,9], Kazunori Nakajima[12],

8 Takeshi Ichinohe[14], Takeshi Nagata[6,15,17], Tomoki Chiba[4,6,7], Fuminori Tsuruta[4,5,6,7*]

9

10 1. Graduate School of Life and Environmental Sciences, University of Tsukuba, 1-1-1
11   Tennodai, Tsukuba, Ibaraki 305-8577, Japan
12 2. Master's and Doctoral Program in Biology, Degree Programs in Life and Earth Sciences,
13   Graduate School of Science and Technology, University of Tsukuba, 1-1-1 Tennodai,
14   Tsukuba, Ibaraki 305-8577, Japan
15 3. College of Biological Sciences, School of Life and Environmental Sciences, University of
16   Tsukuba, 1-1-1 Tennodai, Tsukuba, Ibaraki 305-8577, Japan
17 4. Master's and Doctoral Program in Biology, Faculty of Life and Environmental Sciences,
18   University of Tsukuba, 1-1-1 Tennodai, Tsukuba, Ibaraki 305-8577, Japan
19 5. Master's and Doctoral Program in Neuroscience, Graduate School of Comprehensive Human
20   Sciences, University of Tsukuba, 1-1-1 Tennodai, Tsukuba, Ibaraki 305-8577, Japan
21 6. Ph.D. Program in Human Biology, School of Integrative and Global Majors, University of
22   Tsukuba, 1-1-1 Tennodai, Tsukuba, Ibaraki 305-8577, Japan
23 7. Ph.D. Program in Humanics, School of Integrative and Global Majors, University of
24   Tsukuba, 1-1-1 Tennodai, Tsukuba, Ibaraki 305-8577, Japan
25 8. Graduate School of Pharmaceutical Sciences, The University of Tokyo, 7-3-1 Hongo,
26   Bunkyo-ku, Tokyo 113-0033, Japan
27 9. International Research Center for Neurointelligence (WPI-IRCN), The University of Tokyo,
28   7-3-1 Hongo, Bunkyo-ku, Tokyo 113-0033, Japan
29 10. Institute for Quantitative Biosciences, The University of Tokyo, 1-1-1 Yayoi, Bunkyo-ku,
30   Tokyo 113-0032, Japan
31 11. Department of Anatomy and Cell Biology, Graduate School of Medicine, Nagoya
32   University, Nagoya 466-8550, Japan
33 12. Department of Anatomy, Keio University School of Medicine, 35 Shinanomachi,
34   Shinjuku-ku, Tokyo, 160-8582, Japan.
35 13. Department of Anatomy, The Jikei University School of Medicine, 3-25-8 nishi-shinbashi,
36   Minato-ku, Tokyo, 105-8461, Japan.

14. Department of Infectious Disease Control, International Research Center for Infectious Diseases, Institute of Medical Science, The University of Tokyo, Minato-ku, Tokyo 108-8639, Japan.

15. Information and Communication Research Division, Mizuho Research & Technologies, Ltd. 2-3 Nishiki-cho, Kanda, Chiyoda-ku, Tokyo 101-8443, Japan

16. Department of Life Sciences, School of Agriculture, Meiji University, 1-1-1 Higashimita, Kawasaki, Kanagawa 214-8571, Japan

17. Faculty of Letters, Meiji Gakuin University, 1518 Kamikurata-cho Totsuka-ku Yokohama-shi Kanagawa, 244-8539

* Corresponding author

Tel.: +81-29-853-6887

E-mail: tsuruta.fuminori.fn@u.tsukuba.ac.jp

Abbreviated Title:

Neuronal micronuclei regulate microglial states

53   **Abstract**

54

55   Microglia, resident immune cells in the central nervous system, undergo morphological and

56   functional changes in response to signals from the local environment and mature into various

57   homeostatic states. However, niche signals underlying microglial development and maturation

58   remain largely unknown. In this study, we show that neuronal micronuclei propagate microglia,

59   followed by changing microglial states during the postnatal period. We discovered that neurons

60   passing through a dense region of the developing neocortex give rise to micronuclei and release

61   them into the extracellular space. Moreover, neuronal micronuclei were incorporated into

62   microglia and affected morphological changes. Loss of the *cGAS* gene alleviates effects on

63   micronucleus-dependent morphological changes. Notably, neuronal micronuclei-harboring

64   microglia exhibit unique transcriptome signatures. These results demonstrate that neuronal

65   micronuclei serve as niche signals that produce novel microglial states. Our findings provide a

66   potential mechanism for regulating the microglial state in the early-postnatal neocortex.

67

Introduction

Microglia, the resident immune cells in the central nervous system (CNS), represent the first-line immune defense in the CNS by surveillance with phagocytic scavenging and recruitment of peripheral immune cells[1-3]. In addition, a series of recent studies have established that microglia act as critical players in the development, homeostasis, aging, and a wide range of diseases in the CNS[4,5]. During development, microglia regulate the survival and differentiation of neural progenitor cells (NPCs), migration and maturation of immature neurons, and synapse formation and elimination[6-11]. Microglia also modulate neural activity and circuits in the mature brain[12,13]. As expected by the pivotal and wide-ranged functions, microglial abnormality has been implicated in the majority of neurodevelopmental and neurodegenerative disorders[5,14].

The resident immune cells in the brain consist of a diverse cell population, such as microglia, myeloid cells, and border-associated macrophages (BAMs)/CNS-associated macrophages (CAMs) (hereafter referred to as BAMs). Recent fate mapping analyses have suggested that primitive macrophages arise from erythro-myeloid progenitors (EMPs), migrate into the brain rudiment via circulatory systems at embryonic day (E) 9.5[15], and colonize the brain. Some CD206^{-} progenitor cells colonize the brain and differentiate into microglia[16]. In addition, CD206^{+} macrophages in the ventricle infiltrate into pallium at E12.5 and convert into CD206^{-} microglia, which colonize in the cerebral cortex[17]. After colonization, microglia change their states and exhibit unique, context-dependent, gene expression profiles. Indeed, these profiles are involved in physiological and pathological conditions and affect the acquisition of various microglial functions[18]. Furthermore, BAMs, which reside in the meninges, perivascular space, and choroid plexus, also exhibit unique properties[19,20]. Therefore, understanding the mechanism that determines microglial state is key for elucidating the brain development. Microglial states are thought to be determined by both intrinsic programs and extrinsic signals, such as cytokines, extracellular matrix, and cell-cell interactions. A remarkable aspect of microglia is their dynamic behavior over time. Usually, microglia constantly extend and retract fine-ramified processes and survey the local environments to coordinate with brain homeostasis and neural circuits[21-23]. Moreover, extracellular signals and cell-cell communication locally modulate microglial differentiation, proliferation, and homeostasis[24,25]. Hence, it is likely that context-dependent signals, which are still largely unknown, regulate the microglial characteristics and states.

Micronuclei are small nuclei produced by a chromosome segregation errors and physical stress during cellular migration[26-28]. Micronuclei (MNs) frequently appear in cancer and

4

101 are used as biomarkers[29,30]. MNs are also associated with chromothripsis and epigenetic

102 dysregulation[26,31-34]. Recent studies have revealed that MNs activate the cyclic GMP-AMP

103 synthase-stimulator of interferon genes (cGAS-STING) pathway involved in the innate immune

104 response[35-38]. After damaging the nuclear envelope, micronuclear chromatins are released into

105 the cytoplasm and promote tumor metastasis by activating the cGAS-STING pathway. However,

106 besides these pathological contexts, the physiological roles of MNs have not been fully

107 understood. Moreover, to our knowledge, the roles of MNs in cell-to-cell communications have

108 not been described in any context.

109   In this study, we report that MNs are generated in migrating neurons in the developing

110 mouse neocortex under physiological conditions. The number of micronuclear was increased by

111 inhibiting autophagy. To our surprise, these neuronal MNs are released into the extracellular

112 space close to the surface of the cerebral cortex and incorporated into microglia residing in the

113 superficial layer. The micronucleus incorporation influences morphological changes mediated by

114 cGAS. Strikingly, the bulk RNA-seq analyses have revealed that microglia incorporating MNs

115 increase expression level of extracellular matrix (ECM)-related genes. In addition, gene

116 expression signature resembles BAMs. Therefore, our findings demonstrate that MN is a form of

117 intercellular messenger that mediates neuron-to-microglia communications. These results shed

118 light on the novel mechanisms by which microglial functions and states are modulated by

119 neuronal micronuclei in the early postnatal neocortex.

120

5

Results

Neuronal micronuclei are generated from migrating neurons

Neurons in the cerebral cortex are generated from NPCs in the ventricular and subventricular zone during the embryonic period and migrate to the brain surface. Previously, we observed that MNs exist in the brain of 2-month-old mice[39]. To examine whether MNs also appear in the developing brain, we analyzed the prenatal brain on embryonic day (E) 18.5. We found a couple of MNs in the cerebral cortex (Fig. 1a). Notably, most MNs exist in the superficial layers [marginal zone (MZ) and primitive cortical zone (PCZ)[40]] with few in the cortical plate (CP) (Fig. 1b and 1c). Some of them reside close to nuclei with damaged membranes (Fig. 1d). We next investigated the mechanisms of how MNs are generated in the embryonic brain. Since cancer cells produce MNs via passing a narrow space and deforming nuclei[27,28], we examined whether neuronal MNs are also produced by analogous machinery. To test this idea, we introduced an EGFP-expressing plasmid into cells along a lateral ventricle using *in utero* electroporation (IUE) to label migrating neurons[41]. In the E18.5 cortex, EGFP-labeled neurons were squeezed in a PCZ, generating a micronucleus at the tip of the process (Fig. 1e). Next, to analyze the effect of passing a packed neuronal cell-body-rich area, we produced neuronal aggregates by ectopic expression of Reelin[42]. Consequently, several neurons passing aggregates contained MNs (Fig.1f). This effect was not dependent on Reelin stimulation *in vivo* and *in vitro* (Extended Data Fig. 1a to 1e), implying that micronuclear formation was associated with migrating stress. Then, we investigated whether deforming nuclei by passing them through a narrow space influences micronuclear formation *in vitro*. To do this, we designed the trans-well migration assay (Extended Data Fig. 1f). Neurons migrated from the top toward the bottom side exhibited characteristic morphology with deformed and herniated nuclei (Extended Data Fig. 1g). In addition, more MNs were detected in neurons that passed through the membrane depending on the pore size. (Extended Data Fig. 1h to 1j). To further examine the effect of physical stress, we stressed neurons by pumping cells with a syringe (Extended Data Fig. 1k). We found that the number of MNs was increased when the cell density and stroke frequency were increased (Extended Data Fig 1l and 1m), supporting our idea that MNs formation are caused by physical stress, like passing a narrow and dense region. Next, we examined whether MNs observed in the embryonic period are also present in the neonatal brain as neuron-derived micronuclei. To do this, we observed *NexCre:LSL-SUN1-sfGFP-Myc* mice (*NexCre:LSL-Sun1-GFP*), which can specifically label the nuclear envelope of excitatory neurons[43,44]. The GFP-positive (GFP+) small

154 nuclei were detected at P0 and P7 in Layer 1. Also, these small nuclei were retained until P14

155 (Fig. 1g and 1h). Furthermore, neuronal MNs tended to exist in the motor and somatosensory

156 cortex (Fig. 1i and 1j). The data suggest that neuronal micronuclei produced during brain

157 development reside in the cortical surface, especially in the motor and somatosensory cortices.

158

159 **Neuronal micronuclei are propagated to microglia.**

160 Since MNs are eliminated by autophagy[45], we next analyzed micronuclear behavior in wild-type

161 (WT) and excitatory neuron-specific Atg7 conditional knockout mice (*NexCre:Atg7$^{f/f}$*). Atg7 is

162 an E1-like activating enzyme that plays an important role in autophagosome formation. A defect

163 in the *Atg7* gene leads to a delay in autophagosome formation and perturbs the process of

164 autophagy [46,47]. The number of neuronal MNs in *NexCre:Atg7$^{f/f}$* brain was increased compared to

165 that in WT (Extended Data Fig. 2a and 2b), suggesting that loss of autophagy activity delays

166 MNs turnover during the postnatal period. Surprisingly, we discovered that several MNs were

167 increased in not only neurons but microglia in *NexCre:Atg7$^{f/f}$* mice even though microglial

168 autophagy was normal (Extended Data Fig. 2c and 2d). Thus, we hypothesized that the neuronal

169 MNs are transferred from neurons to microglia (Fig. 2a). To examine this, we first analyzed

170 whether MNs exist in the extracellular space *in vitro* and *in vivo*. Consequently, several MNs

171 were detected outside primary cultured neurons. In addition, we observed micronuclei in the

172 MAP2$^-$ and S100β$^-$ regions *in vivo* (Fig. 2b and 2c). Notably, some of the MNs were surrounded

173 by membrane-like structures (Fig. 2d), implying that these MNs are contained in extracellular

174 vesicles.

175 Then, to investigate whether MNs are released from neurons, we developed an *in vitro*

176 assay system. First, we biochemically collected MNs from a conditioned medium and identified

177 the fraction containing neuronal MNs (Fig. 2e and 2f). Notably, extracellular MNs were

178 increased when lysosomal activity was inhibited without apoptosis (Extended Data Fig. 2e to

179 2g), suggesting that a defect in lysosomal activity promotes micronuclear secretion. We next

180 attempted to identify the content of MNs. Using the liquid chromatography and mass

181 spectrometry (LC/MS) analysis, we found several nuclear proteins, such as various Histone

182 proteins (H1.4, H2A type 2-C, H2B type 1-B, H2A.V, H3.3, H1) and Histone-binding protein

183 RBBP7. We also identified several components, including TRiC complex proteins (TCP1α,

184 TCP1β, TCP1δ, TCP1ε, TCP1γ, TCP1ζ, TCP1θ), Tubulin proteins (Tubulin α1A, α1C, αl3, β2A,

185 β2B, β3, β4A, β5), and Rab family proteins (Rab1A, Rab1B, Rab2A, Rab3A, Rab11B, Rab15,

186 Rab35) (Fig. 2g and 2h, Extended Data Table 1). To confirm whether these proteins reside in

187 MNs, we harvested extracellular MNs, adhered to the coverslips, and conducted immunostaining

188 assay. Tubulin and Rab35 signals were observed in the extracellular MN-like structure

189 (Extended Data Fig. 2h and 2i). We also confirmed that TRiC protein complexes reside in MNs

190 in primary cultured neurons using the trans-well analysis (Extended Data Fig. 2j). Moreover,

191 small amounts of Tubulin were colocalized with the neuronal MNs *in vivo* (Extended Data Fig.

192 2k), suggesting that the proteins identified by LC/MS analysis are potential candidates for the

193 component of MNs. Previously, it has been shown that TRiC complex proteins, TCPβ, serve as a

194 receptor of LC3 and promote autophagosome formation[48]. Because LC3 was localized on the

195 MNs in the cerebral cortex (Extended Data Fig. 2l), the TRiC protein complex may serve as a

196 potential mediator linking MNs to autophagosome formation associated with autophagic

197 secretion (Extended Data Fig. 2m).

198   Next, we investigated whether extracellular MNs were incorporated into microglia.

199 To examine this, we developed an *in vitro* micronuclear transfer assay system (Extended Data

200 Fig. 3a) and observed the MN-like structure in microglial cell line, BV2 cells (Extended Data

201 Fig. 3b and 3c). Using this system, we analyzed the timing of micronuclear incorporation. BV2

202 cells took neuronal MNs (GFP$^+$-MNs) efficiently at two hours after stimulation with conditioned

203 medium (CM) from *NexCre:LSL-SUN1-sfGFP-Myc* neurons. Whereas the population of MNs in

204 BV2 cells was high at two hours and six hours after stimulation (Extended Data Fig. 3d and 3e),

205 suggesting that microglia take neuronal MNs, followed by disappearing the nuclear envelope or

206 inducing novel MNs derived from microglial nuclei. To verify whether the increase in microglial

207 MNs depends on extracellular MNs, we filtered the CM to remove extracellular MNs. Treatment

208 of filtered CMs did not induce the formation of MNs (Extended Data Fig. 3f and 3g), implying

209 that extracellular MNs are necessary for increasing the number of MNs in microglia. Next, to

210 investigate whether propagation of MNs is observed *in vivo*, we observed

211 *NexCre:LSL-Sun1-GFP* brain. As we expected, most GFP$^+$-MNs existed in Layer 1. In addition,

212 some MNs were taken up by microglia (Fig. 2i - 2j). Moreover, we conducted a cortical slice

213 culture imaging using microglia and nuclear labeled mice (*Cx3cr1-EGFP;H2B-mCherry*

214 mice)[49,50]. Intriguingly, several motile MNs were detected, and some seemed to be taken by

215 microglia in the superficial area of cerebral cortex (Extended Data Fig. 3h, Extended Data Video

216 1). These data are consistent with the possibility that micronuclear propagation regulates

217 microglial characteristics close to the surface of the cerebral cortex.

218

219 **Micronuclei affect microglial morphology during the early-postnatal period via cGAS.**

220　To investigate whether MNs regulate microglial characteristics, we first analyzed microglial

221　morphology. The microglia gradually change their shapes and mature by P14[51,52]. Because MNs

222　were mainly observed in Layer 1, we first examined the involvement in the layer specificity of

223　microglial complexity. Microglia in Layer 1 exhibited slightly less complexity than those in

224　other layers (Extended Data Fig. 4a - 4d), implying a potential link between MNs and microglial

225　complexity. Next, we analyzed whether incorporated MNs affect microglial complexity (Fig. 3a).

226　The process length in microglia is distinguishable according to the existence of MNs, although

227　microglia with GFP$^-$-MNs show more simplified morphology (Fig. 3b - 3d). Moreover, there

228　were only minor differences observed in the expression levels of microglial marker genes (*Cd68*,

229　*Tmem119*, *P2ry12*) between cells with and without MN, and no significant biological

230　implications were observed (Extended Data Fig. 5a - 5f). These data suggest that micronuclear

231　propagation changes a hallmark of microglia, such as morphology, regardless of representative

232　microglial gene expression. The question is how MNs regulate microglial states. MNs have been

233　reported to be recognized by cGAS after exposing chromatin DNA[35-38]. Since cGAS is mainly

234　expressed in microglia in the brain[53] (Extended Data Fig. 6a), we analyzed conventional *cGAS$^{-/-}$*

235　mice brains. The morphological complexity was increased in *cGAS$^{-/-}$* microglia at the early stage

236　(Extended Data Fig. 6b - 6e), implying that cGAS is crucial for regulating morphological

237　complexity. Notably, cGAS deficiency cancels the effect of MNs-regulated morphological

238　changes (Fig. 3e - 3j, Extended Data Fig. 6f - 6i). These data suggest that cGAS is involved in

239　MN-dependent morphological changes.

240

241　**Neuronal micronuclei alter a hallmark of microglia**

242　Because neuronal MNs seem to affect the microglial state, we purified CD11b$^+$ GFP$^\pm$ microglia

243　from the postnatal brains of *NexCre:LSL-Sun1-GFP* mice. The mRNAs isolated from microglia

244　were analyzed by bulk RNA-sequencing (RNA-seq) analysis, and the differentially expressed

245　genes (DEG) were determined using *edgeR* software[54,55] (Fig. 4a and 4b, Extended Data Fig. 7a,

246　Extended Data Table 2). Due to the presence of SUN1-GFP in MN, we first divided the

247　microglial subpopulation into two groups [GFP$^-$ microglia and GFP$^+$ microglia]. Since the

248　population of GFP$^+$ microglia was not converged, we further subdivided GFP$^+$ microglia into

249　two groups; Type 1 (low signal of GFP, GFP^{Low}) and Type 2 (high signal of GFP, GFP^{High}) (Fig.

250　4c). RNA-seq analysis revealed that GFP^{High} microglia possessed various neuronal mRNA

251　(*MAP1b*, *MAP2*, *Rian*, *Grin2b*, *Pgm2l1*) (Extended Data Fig. 7b - 7r). Since phagocytic

252　microglia often possess mRNAs of engulfed cells[56], we speculated that neuronal mRNA in

253   GFP^{High} microglia are derived from phagocytosed apoptotic neurons. In contrast, as little

254   neuronal mRNA was detected in GFP^{Low} microglia, we analyzed these GFP^{Low} microglia as

255   microglia incorporated neuronal MNs. Intriguingly, GFP^{Low} microglia increased the expression

256   of ECM-related genes compared to both GFP^{Neg} and GFP^{High} microglia (Fig. 4d). The genes

257   identified in GFP^{Low} microglia were partially shared with the genes which were highly expressed

258   in the BAMs (*CD206*, *Dab2*, *Stab1*, *Slc40a1*) [16,57,58] (Fig. 4e and 4f, and Extended Data Fig. 8a -

259   8v), suggesting that neuronal MNs are involved in changing microglial state. Indeed, some

260   microglia with MNs slightly increased the expression of CD206 (Fig. 4g and 4h). Moreover, we

261   found BAMs in the meninges also incorporated neuronal MNs with few chromatin (Fig. 4i).

262   These data suggest that neuronal MNs regulated-microglial signature may be controlled by

263   multiple pathways.

264

Discussion

265

266

267   So far, MNs have been described mainly in the context of tumorigenesis, in which they emerge

268   by genomic instability and cellular migration. DNA fragments of the MNs are released to the

269   cytoplasm, and cell-autonomously accelerate the malignancy phenotype[59]. In this study, however,

270   we have revealed the existence of MNs in a physiological context and their role in the

271   developmental regulation of microglia. Remarkably, our results demonstrated that MNs

272   generated in neurons are released into the extracellular space and incorporated into microglia,

273   regulating microglial signatures (Fig. 4j). Our study thus unexpectedly unveils a novel form of

274   intercellular communication via MNs.

275   The finding in this study is that incorporating MNs into microglia changes the

276   properties of those microglia. Notably, the ECM-related genes were upregulated in MNs$^+$

277   microglia. Furthermore, the gene expression profile of MNs$^+$ microglia partially overlapped with

278   that of BAMs. Therefore, we hypothesized that neuronal MNs might endow microglia with

279   properties similar to BAMs. BAMs reside in the meninges, perivascular spaces, and choroid

280   plexus. Fate mapping analyses have revealed that EMPs from the yolk sac differentiate into

281   maturating macrophages[60]. Then, they change into either parenchymal microglia or BAMs

282   depending on whether EMPs are stimulated by TGFβ signaling[16]. However, understanding the

283   functions of BAMs that underlie brain development and homeostasis has been hindered due to a

284   low number of cells. On the other hand, despite the limited number of studies, several groups

285   have reported the biological relevance of BAMs. First, ablating BAMs using pharmacological

286   inhibitors increased aberrant ECM accumulation[61]. Indeed, the BAMs-residing areas, such as

287   meninges, choroid plexus, and perivascular spaces, are surrounded by various ECM proteins.

288   Thus, BAMs may regulate the architecture of the border region through the precise expression of

289   ECM-related proteins. Perivascular macrophages have been reported to repair a small lesion in

290   the vessel, suggesting that BAMs contribute to maintaining and repairing the brain vessels[62].

291   Here, we found that microglia taken up neuronal MNs change ECM-related gene expressions

292   (*Col1a1*, *Col1a2*, *Col3a1*), implying that extracellular MNs are one of the potential mediators

293   that alters the microglial signature during early-postnatal stages. Because the meningeal

294   macrophages seem to transit to the perivascular macrophages during the postnatal stages[63], it is

295   likely that microglia or meningeal macrophages taken up MNs migrate toward the perivascular

296   region. We also observed that various neuron-specific genes are expressed in GFP^{High} microglia.

297   Since early postnatal microglia are mostly reactive states and maintain the brain environment

11

298   through phagocytosing apoptotic neurons, it is likely that GFP[High] microglia may also compose

299   GFP[+] neuronal nuclei derived from apoptotic neurons. Meanwhile, the genes identified in

300   RNA-seq analysis, such as Nrgn and Marcksl1, are expressed in non-neuronal cells, including

301   microglia. So, we presume that some may be target genes induced by MNs.

302   The mechanisms that underlie the release of MNs have not been clarified. While the

303   autophagy pathway mainly plays a vital role in cargo degradation, either acceleration or

304   inhibition of autophagic machinery modulates the secretion pathway[64]. In this study, we found a

305   couple of potential targets that underlie MNs secretion associated with autophagy, such as TCP

306   family proteins and Rab family proteins. It has been shown that treatment with bafilomycin,

307   which can inhibit autophagosome-lysosome fusion via perturbed pH in the lysosome, promotes

308   aggregated α-synuclein secretion[65]. Because TRiC protein subunit, TCPβ, bridges between

309   aggregated protein and LC3[48], it is possible that MNs are also secreted by analogous machinery

310   mediated by TCP subunits. Also, Rab family proteins, Rab11 and Rab35, have been reported to

311   be involved in regulating exosome secretion[66,67]. Since we identified these proteins as potential

312   components in our proteomics screening, these Rab family proteins may also serve as regulatory

313   factors that control MNs secretion. The ATG-conjugation system plays a critical role in the

314   degradation of the inner autophagosomal membrane but not in the formation of an

315   autolysosomes[68]. While we cannot completely rule out the possibility that the extracellular

316   vesicles are apoptotic bodies formed by dying neurons, we speculate that the extracellular

317   vesicles were switched from the autophagy degradation pathway to the secretory pathway and

318   subsequently released due to a loss of autophagy function (see Extended Data Fig. 2m).

319   To date, EVs, including microvesicles, have been identified as key mediators of

320   intercellular communication[69]. Microvesicles are similar in size to extracellular MNs (1.0 μm to

321   3.0 μm), and are released from the plasma membrane via a budding process, transferring cargo to

322   target cells. The ESCRT III complex is crucial for the scission of vesicles from the membrane[70]

323   and regulates membrane repair by releasing the damaged patch to the extracellular region[71,72].

324   Thus, it is likely that the ESCRT-III complex may control extracellular MNs production through

325   the budding process, which is linked to the autophagy-dependent pathway. Intriguingly, EVs

326   transport organelle intercellularly in the brain. Mitochondria are among the organelles that are

327   transported by EVs under both neurodegenerative or ischemic conditions[73,74]. Hence, EVs

328   containing MNs may represent a novel type of microvesicle that modulate microglial signature.

329   In addition to microvesicles, various types of EVs, including exosomes, have been reported to

330   contribute to cell-cell communication in the central nervous system[69]. Exosomes are small

12

331   vesicles (ranging from 100 nm to 1.0 μm) that are released from the multivesicular bodies and

332   carry both RNAs and proteins to target cells. Under pathogenic conditions, glia propagate the

333   pathogenic proteins through exosomes[75]. Components of the nucleus, such as nuclear protein

334   (Lamin A/C and Histone H2B) and chromatin, are transferred from MNs to exosomes and

335   released to the extracellular space[76]. Although the size of MNs is larger than the exosome, a

336   comparative analysis between the exosome and microvesicle is an exciting study, and further

337   validation is required.

338   Recent research suggests that cGAS is a redundant DNA sensor in the cytoplasm[77].

339   Previous studies have shown that cGAS in microglia is involved in ischemia, virus infection, and

340   neurodegeneration[78].   Since   cGAS   induces   IFNβ   expression   by   activating   the

341   cGAS-STING-IRF3 pathway, we investigated the link between incorporating MNs and IFNβ

342   expression. However, we did not obtain clear data with or without MNs *in vivo*. While we cannot

343   rule out the possibility of technical difficulties to detect endogenous IFNβ, we also speculate an

344   IRF3-independent mechanism. Previous studies have reported that cGAMP, an intercellular

345   mediator, is transported via specific transporters[79-81]. Hence, it is intriguing that released cGAMP

346   regulates microglial characteristics via an autocrine pathway. Furthermore, as we observed that

347   certain MNs lack chromatins, it is likely that the MN-dependent, cGAS-independent pathway is

348   also involved in regulating microglial signature .

349   During embryonic development, microglia are believed to migrate to the pial surface in

350   response to signals from meninges[82]. As the microglial signature is region- and stage-specific, it

351   is possible that MNs in the superficial layer contribute to generating the unique microglial

352   signature. In the cerebral neocortex, neurons form six-layer structures. In the PCZ, a dense

353   region in the superficial CP, migrating neurons contain intracellular MNs with deformed nuclei[40].

354   We often observed here that intracellular MNs reside in the process of migrating neurons with

355   deformed nuclei in the PCZ. Thus, we hypothesize that physical stress may trigger the formation

356   of intracellular MNs in neurons, as the number of MNs$^+$ neurons increases when neurons pass

357   through narrow spaces *in vitro*. Similar to cancer cells[27,28], migrating neurons may receive

358   physical stress and nuclear deformation, which can induce changes in their epigenetic state[83].

359   Therefore, it is likely that physical stress in the neuronal nucleus provides a biological cue that

360   affects the gene expression profile associated with the microglial states.

361   In conclusion, our study demonstrates that MNs are generated from migrating neurons

362   and released during the early postnatal period. These MNs are subsequently taken up by

363   microglia, and their presence is associated with cGAS activity and alterations in the microglial

13

364   state. Our findings provide novel insights into the relevance of the propagation of neuronal MNs

365   and microglial diversity during early-postnatal stages.

366

Materials and Methods

Mice

The Crl:CD1(ICR) mice were obtained from Japan SLC, Inc. (Shizuoka Japan). The B6.Cg-Atg7[tm1Tchi] (Atg7[f/f]) mice have been described previously[46]. The B6;129-Gt(ROSA)26Sor[tm5(CAG-Sun1/sfGFP)Nat/J] (*LSL-Sun1-GFP*), B6.Cg-Gt(ROSA)26Sor[tm9(CAG-tdTomato)Hze/J]), B6(C)-cGAS[tm1d(EUCOMM)Hmgu/J] (*cGAS^{-/-}*), and B6.129P2(Cg)-Cx3cr1[tm1Litt]/J mice were obtained from the Jackson Laboratory (the stock #: 021039, 007909, 026554, and 005582 respectively)[43,44,49,84]. R26-H2B-mCherry (accession #: CDB0239K) mice were previously described[50,85]. To generate *NexCre:Atg7[f/f]* mice and *NexCre:LSL-Sun1-GFP* mice, the *Atg7[f/f]* mice and *LSL-Sun1-GFP* mice were crossed to the Neurod6[tm1(cre)Kan] (NexCre)[86], respectively. All of the animal experiments were conducted according to the university guidelines for animal care. This study was approved by the Animal Experiment Committee in the University of Tsukuba (the approval numbers:18-257, 19-340, 20-438, 21-443, 22-427).

Cell culture

BV2 cells were cultured in DMEM/nutrient mixture F-12 (DMEM/F12; Thermo Fisher Scientific) containing 10% fetal bovine serum (FBS), 100 units penicillin, and 100 mg streptomycin (P/S; Thermo Fisher Scientific) at 37□ with 5% CO_2[87]. Neuro2A cells were cultured in EMEM (FUJIFILM Wako) containing 10% FBS and P/S. HEK293T cells were cultured in DMEM (FUJIFILM Wako) containing 5% FBS and P/S[88]. Primary cortical neurons were prepared from E13.5-14.5 ICR mice or *NexCre:LSL-Sun1-GFP* mice as previously described[89]. Briefly, mouse cortical neurons were plated on coverslips coated with either 0.01875% Poly (ethylenimine) solution (SIGMA) and cultured in Neurobasal medium (Thermo Fisher Scientific) containing B-27 supplement (Thermo Fisher Scientific) and P/S. Neurons were maintained for 5 - 7 days at 37□ with 5% CO_2 and were subjected to *in vitro* MNs transfer assay and trans-well migration assay.

Antibodies, materials, and plasmids

For immunofluorescence, anti-MAP2 (MAB378, Merck Millipore, 1:500), anti-Iba1 (#019-19741, WAKO, 1:1000), anti-GFP (#598, MBL, 1:500), anti-GFP (ab13970, abcam, 1:1000), anti-RFP (#600-401-379, Rockland, 1:3000), anti-Cleaved Caspase-3 (Asp175) (5A1E,

15

400 CST, 1:500), anti-CD68 (FA-11, Biolegend, 1:500), anti-Lamin B1 (ab16048, abcam, 1:500),

401 anti-S100β (ab52642, abcam, 1:1000), anti-Rab35 (11329-2-AP, Proteintech, 1:1000),

402 anti-Tubulin (DM1A, SIGMA, 1:1000), anti-LC3 (PM036, MBL, 1:1000), anti-CD206 (AF2535,

403 R&D systems, 1:200), anti-P2ry12 (AS-55043A, AnaSpec, 1:1000), anti-Tmem119 (ab209064,

404 abcam, 1:600) were used as the primary antibody. For immunoblotting, anti-GFP (#598, MBL,

405 1:1000), anti-Tubulin (SIGMA, DM1A, 1:1000), and anti-Lamin B1 (ab16048, abcam, 1:1000)

406 were used as the primary antibody. Bafilomycin A1 (BafA) was purchased from CST (#54645).

407 The recombinant Reelin (3820-MR/CF) was purchased from R&D Systems. The full-length

408 mouse Reelin cDNA and pCAGGS1 plasmid containing a CAG promoter were kindly provided

409 by Dr. T. Curran (Children's Mercy Kansas City) and Dr. J Miyazaki (Osaka University),

410 respectively.

411

412 *In utero* **electroporation**

413 An *in utero* electroporation was modified as previously described[90]. Briefly, the day detected

414 virginal plug was defined as E0, and the day of birth was defined as P0. The pregnant ICR or

415 C57BL/6 mice (E14.5) were anesthetized with isoflurane. The mother mouse was warmed using

416 a heater to maintain body temperature. After a midline laparotomy was performed, the embryos

417 were pulled out. The 1.0 μl of DNA (5 μg/μl in water) together with the 0.01% Dye Fast Green

418 (SIGMA) was injected through the uterine wall into one of the lateral ventricles of the cerebral

419 cortex by the glass capillary. For injection, the glass capillaries were made from the thin-walled

420 glass capillary (GD-1, Narishige) utilized by the capillary puller (PC-100, Narishige). An *in*

421 *utero* electroporation was performed using an electroporator (NEPA21, NEPAGENE). The

422 electronic pulse (poring pulse 50V, pulse length 50 msec, pulse interval 950 msec, 4 times and

423 transfer pulse 50V, pulse length 50 msec, pulse interval 950 msec, 4 times) were applied with a

424 forceps-type electrode (CUY650P5, NEPAGENE). The plasmids of pGAG-EGFP and

425 pCAG-Reelin were injected in one side to minimize the damage to the brains.

426

427 **Immunohistochemistry**

428 The brains were fixed by perfused with 4% paraformaldehyde (PFA) in phosphate buffered

429 saline (PBS) and fixed with the same fixative solution overnight. After 30% sucrose in PBS

430 infiltration, the samples were embedded in Tissue-Tek OTC compound (SAKURA) and sliced at

431 a 50 μm thickness by the cryostat (Leica Biosystems). Free-floating slices were permeabilized

432 and blocked with PBS containing 0.25% Triton X-100 and 5% bovine serum albumin

433   (BSA). Primary antibodies were incubated in PBS containing 0.1% Triton X-100 and 5% BSA

434   for 3 days (anti-MAP2 antibody) or 1 day (all others) at 4°C. Immunostaining was detected using

435   Alexa 488, Alexa 594, or Alexa 647 fluorescent secondary antibody (Thermo Fisher Scientific,

436   1:1000), incubated in PBS containing 5% BSA for 1 hour at room temperature. Slices were

437   counterstained with DAPI solution (Dojindo) and mounted in VECTASHIELD Mounting

438   Medium (Vector Laboratories). Tissue specimens were observed using the confocal laser

439   scanning microscope (LSM700, Carl Zeiss) with 20x (Plan-Apochromat 20x/0.8 M27) and 40x

440   (Plan-Apochromat 40x/1.3 Oil DIC M27) objective. The diode excitation lasers (Diode 405,

441   Diode 488, and Diode 555) were operated and directed to a photomultiplier tube (LSM T-PMT,

442   Carl Zeiss) through a series of bandpass filters (Ch1:BP420-475 + BP500-610, Ch2:BP490-635,

443   and Ch3:BP585-1000). The Z-stack images (interval: 1 μm per image) were acquired using ZEN

444   software (Carl Zeiss). The microglial morphological were assessed by the Image J skeleton and

445   fractal analysis[91]. For the high throughput imaging in Figure 1i, the fluorescence images were

446   obtained using the Thunder imaging systems (Leica) equipped with 20x objective (HC PL

447   Fluotar L 20x/0.4 CORR PH1), the diode excitation laser (395 and 470), and filter set (Ex391/32,

448   DC 415, Em 435/30 for DAPI, Ex479/33, DC 500, Em519/25). The fluorescent images were

449   decoded by Thunder imaging system for computational clearing (Leica Application Suite X

450   3.7.0)

451

452   **Immunocytochemistry**

453   Primary cortical neurons were plated at 1.0×10^6 cells/well on the trans-well (Corning, 12 mm

454   Trans-well with 3.0 µm Pore Polycarbonate Membrane Insert, 3402) for 3 days. The

455   polycarbonate membranes (top and bottom) were coated with 0.01875% Poly (ethylenimine)

456   solution (SIGMA) for 1 day. Only the bottom sides were recoated by 1.42 µg/ml laminin

457   (SIGMA) for 1 day. Neurons were stained with anti-MAP2 and anti-Lamin B1 antibodies and

458   subjected to analyzing MNs using MATLAB-based program for quantifying MNs (Calculating

459   automatic MNs distinction: CAMDi)[39]. Neuro2A cells (5.0×10^4 cells) were loaded into a

460   syringe fitted with a needle [Dentronics, No.32 (0.26 mm x 12 mm), Cat# HS-2739B] and were

461   subject to single or ten strokes. Neuro2A cells were plated on the cover glass and were incubated

462   for one day. Cells were then stained with Hoechst and subjected to analyzing MNs using

463   CAMDi. BV2 cells were plated at 2.5×10^4 cell/cm^2 density on glass coverslips (15 mm

464   diameter, Matsunami Glass) in 12 well plates. Conditioned medium was added 1

465   day after plating. Cells were fixed with 4% PFA in PBS for 10 min at room temperature. BV2

17

466 cells on coverslips were blocked in 0.25% Triton X-100 in blocking solution (5% BSA in PBS)

467 for 30 min at room temperature and then incubated with primary antibodies diluted in blocking

468 solution for overnight at 4°C. After washing with PBS, the cells were incubated with Alexa Fluor

469 Plus secondary antibodies (Thermo Fisher Scientific, 1:1000) or Dylight Fluorochrome

470 conjugated secondary antibodies (abcam, 1:1000) diluted in blocking solution for 30 minutes at

471 room temperature. The nuclei were stained with 10 μg/ml Hoechst 33342 (SIGMA) or 1.0 μg/ml

472 DAPI. The coverslips were mounted onto slide glasses using FLUOROSHIELD Mounting

473 Medium (ImmunoBioScience). Fluorescent images were obtained using the fluorescence

474 microscope (BZ-9000, Keyence) with 40x (PlanApo 40x/0.95) and 100x (PlanApo VC 100x/1.4

475 Oil) objective and a charge-coupled device camera (Keyence). A proper wavelength was selected

476 using fluorescence filter cubes；DAPI [Ex 360/40, DM 400, BA 460/50] (Keyence), GFP-B [Ex

477 470/40, DM 495, BA 535/50] (Keyence), mCherry-A [Ex FF01-562/40-25, Di

478 FF593-Di02-25x36, Em FF01641/75-25](Opto-Line, Inc). Other fluorescent images were

479 obtained using the confocal laser scanning microscope (LSM700, Carl Zeiss) with 20x

480 (Plan-Apochromat 20x/0.8 M27) and 40x (Plan-Apochromat 40x/1.3 Oil DIC M27) objective.

481 The diode excitation lasers (Diode 405, Diode 488, and Diode 555) were operated and directed

482 to a photomultiplier tube (LSM T-PMT, Carl Zeiss) through a series of bandpass filters

483 (Ch1:BP420-475 + BP500-610, Ch2:BP490-635, and Ch3:BP585-1000).

484

485 **Immunoblot analysis**

486 To characterize the extracellular MNs released from neurons, the cultured media were collected

487 from primary cortical neurons of *NexCre:LSL-Sun1-GFP* mice or ICR mice, and isolated by

488 differential centrifugation. The collected media was subjected to a centrifugation step of 400 x g

489 for 10 min at room temperature to remove cells. Next, the supernatant was centrifuged at 2,000 x

490 g for 20 min at 4□ to remove apoptotic bodies. For the collection of large factors, the

491 supernatant was centrifuged at 15,000 x g for 40 min at 4□. This supernatant was next subjected

492 to ultracentrifugation at 120,000 x g for 2 h at 4□ in a SW 41 Ti Rotor Swinging-Bucket rotor

493 (Beckman Coulter), and the pellets collected as small factors like exosome. Cellular proteins and

494 extracellular proteins from media were extracted with 100 μl of ice-cold RIPA lysis buffer (10

495 mM Tris-HCl [pH7.5], 150 mM NaCl, 1 mM EDTA, 1% NP-40, 0.1% sodium deoxycholate,

496 0.1% SDS, and 1 μM dithiothreitol [DTT]) and 30 μl of that, respectively. After

497 SDS-polyacrylamide gel electrophoresis, each sample was transferred to a polyvinylidene

498 difluoride membrane (Pall). The membranes were blocked in 5% skim milk for 60 min at room

499   temperature and were then incubated overnight at 4°C with the primary antibodies. After

500   washing with PBS, the membranes were incubated for 1 hour with the peroxidase-conjugated

501   secondary antibodies. The signals on the membrane were detected by Chemi-Lumi One Super

502   (Nacalai tesque)

503

504   ***In vitro* micronuclei transfer assay**

505   Primary cultured cortical neurons purified from E13.5-14.5 ICR mice embryonic cerebral cortex

506   were plated at 1.0×10^6 cells/well (12-well plate) and incubated for 7 days and were then

507   incubated with DMSO or 300 nM BafA at 37°C for 3 h. Neurons were rinsed with PBS twice

508   and refreshed with Neurobasal medium containing B27. After a 3 h incubation, the dead cells

509   were removed using centrifugation (pelleted at 800 × g, 5 min, 4). To remove MNs from the

510   conditioned medium, the medium was filtrated through 0.22 μm pore PES filters (Millipore).

511   BV2 cells were treated with the conditioned medium for 2 - 6 hours and subjected to an *in vitro*

512   MNs assay. HEK293T cells were plated at 1.0×10^6 cells/ dish (6 cm dish) and incubate for 1 day.

513   Cells were then transfected with either Reelin-HA or control plasmid using 1.0 mg/ml

514   polyethyleneimine MAX (Polyscience). After 2 days, the conditioned medium was collected and

515   were centrifuged at 8,000 rpm for 5 min to remove the debris. Primary cultured cortical neurons

516   [5 day in vitro (DIV)]were treated with the conditioned medium for 6 hours and were then

517   subjected to a MNs assay.

518

519   **Micronuclei analysis**

520   FIJI ImageJ software (NIH) and ZEN (Carl Zeiss) are used for converting each Z-stack image

521   (interval; 1 μm per image, a total thickness of images staining with MAP2; 10 to 15 μm, a total

522   thickness of images staining with Iba1; 30 to 50 μm) to a single TIFF file. The data were

523   imported into the MATLAB-based program CAMDi for quantifying MNs[39]. Briefly, the rate of

524   overlap area of the nucleus is defined as 0.5. The imported data are conducted binarization and

525   are determined the threshold of each color. After making the binary images, the merged areas are

526   extracted according to the threshold, followed by quantification of the number, area, and volume.

527   It has been reported that the maximum size of micronucleus is defined as one-third of the main

528   nucleus[92,93]. The major axis of neuronal nuclei is approximately 12 to 15 μm. On the other hand,

529   we rarely observed large sizes of nuclei (approximately less than 18 μm), but they resided in the

530   brain. Thus, the extra nuclei within a major radius of 3.0 μm were defined as MNs.

531

Transmission electron microscope

For the cellular electron micrograph, BV2 cells were collected after conducting a micronuclear transfer assay (see [*in vitro* micronuclear transfer assay] section) and subjected TEM imaging. Briefly, cells were fixed with 2.5% glutaraldehyde in 0.1M phosphate buffer at 4°C for 30 min. After washing with phosphate buffer, cells were fixed with 1.0% osmium tetroxide 4°C for 90 min. Next, cells were dehydrated with ethanol and were then reacted with propylene oxide for 20 min twice. After obtaining the thin section, the samples were stained with 2% uranyl acetate and lead citrate. The images were obtained using a JEM 1400 (JOEL). For the brain electron micrograph, the postnatal ICR mice (P0) were perfused with fixative solution (4% PFA, 2.5% glutaraldehyde, 0.1% picric acid, 0.05 mg/ml ruthenium red in 0.1M phosphate buffer [7.2]). The mice brains were post-fixed for 1-2 hours at 4°C using a fixative solution. After washing with phosphate buffer, the brain sections (coronal section, 300 μm) were prepared with a vibratome. The sections were then fixed again with 1% osmium tetroxide and 0.05% ruthenium red for 30 min at room temperature. After sequential dehydration with ethanol solutions and replacement with n-butyl glycidyl ether, the extra-thin sections (60-80 nm) were obtained using ultra cut UCT (Leica) and stained with 2% uranyl acetate and lead citrate. The images were obtained using a JEM 1400 (JEOL).

Mass spectrometry and data analysis

The extracellular MNs were collected by ultracentrifugation (see the [immunoblot analysis] section). After adding 90 μl of AB buffer (100 mM ammonium bicarbonate buffer [90%]/Acetonitrile [10%]), the samples were added 4 μl of 100 mM DTT/10% acetonitrile/100 mM AB buffer and incubated at 37°C for 60 min. The samples were added 10 μl of 100mM Iodoacetamide/10% Acetonitrile/100mM AB buffer and incubated at 37°C for 30 min. The samples were then subjected to trypsin digestion and injections into LC/MS (Zaplous ADV Q-Exactive system, AMR Inc.). The raw data were categorized using the DAVID Bioinformatics Resources 6.8 database (https://david.ncifcrf.gov/)

FACS analysis

Isolation of GFP[Neg], GFP[Low], and GFP[High] microglia were performed as previously described[52,94]. The cortices of the *NexCre:LSL-Sun1-GFP* mice (P8 to P10) was homogenized using a syringe with 23G and 27G needles, sequentially in 500 μL of PBS including 0.2% DNaseI (Takara). The solution was mixed with 145 μL of Debris Removal Solution (Miltenyi), and 600 μL of PBS was

20

565 layered on it. The tube was centrifuged at 3,000 x g for 10 min at 4°C. After removing upper

566 layer including debris, the solution was mixed with 600 μL of PBS and centrifuged at 1,000 x g

567 for 10 min at 4°C. After removing supernatant, the pellet was resuspended with 200 μL of PBS

568 including 0.2% BSA, added anti-CD11b conjugated with APC-Cy7 (BioLegend, #101226) and

569 anti-CD45 conjugated with PerCP-Cy5.5 (BioLegend, #109828), and placed on ice for 10 min.

570 The solution was mixed with 60 μL of Debris Removal Solution, and 260 μL of PBS was

571 layered on it. After removing supernatant, the pellet was resuspended with 200 μL of PBS

572 including 0.2% BSA and subjected to FACS with the FACSAria instrument (Becton Dickinson).

573 Gating strategies are presented in Extended Data Fig 7a.

574

575 **Live imaging in cortical slice culture**

576 An *in vivo* imaging was modified as previously described[17]. Live imaging of cortical slice culture

577 was performed using forebrains isolated from *Cx3cr1-EGFP*^{+/-};*H2B-mCherry*^{+/-} mice at P3. The

578 forebrains were embedded in 2% agarose gel and sliced at 400 nm using a vibratome. These

579 brain slices were placed on the glass-bottom dishes (Iwaki, Cat#3910-035), fixed in collagen gel

580 (Cellmatrix Type I-A [Collagen, Type I, 3 mg/mL, pH 3.0], Nitta Gelatin, Cat#KP-2100), and

581 added in a medium composed of DMEM/F12 (Sigma) containing 5% FBS (Invitrogen), 5%

582 horse serum (HS) (Invitrogen), penicillin/streptomycin (50 U/ml, each) (Meiji Seika Pharma Co.,

583 Ltd.), N-2 Supplement (Thermo Fisher Scientific, Cat#17502001), and B-27 Supplement without

584 vitamin A (Thermo Fisher Scientific, Cat#12587010). Time-lapse *in vivo* imaging was conducted

585 using a CSU-X1 confocal microscope (Yokogawa, Tokyo, Japan) with 40x (Olympus

586 LUMPLanFL N 40x / 0.80W) objective. Chambers for culture were filled with 40% O_2 and 5%

587 CO_2. The Z-stack images (z-stack pitch;1.5 μm) were acquired using MetaMorph software

588 (Molecular DEVICES). Each image is taken every 5 min. The z-stack images were expanded

589 using a MATLAB program, and the appropriate MNs were identified in each image by analyzing

590 above and below images individually.

591

592 **RNA-seq analysis**

593 The library for RNA-seq analysis was constructed with SMART-seq Stranded Kit (Takara) using

594 10,000 isolated cells by FACS and subjected to sequencing on the Illumina HiseqX platform to

595 yield 151-base paired end reads. Approximately 10 to 20 million sequences were obtained from

596 each sample. Sequences were mapped to the reference mouse genome (mm10) with hisat2

597 software (10.1038/s41587-019-0201-4). Only uniquely mapped fragments with no base

21

598   mismatches were used for the analysis. Gene expression was quantitated as fragments per

599   kilobase of exon per million mapped reads (FPKM) on the basis of Genecode M20 (mm10).

600   DEGs between GFP^{Neg}, GFP^{Low}, and GFP^{High} groups were determined as genes whose FDR were

601   lower than 0.05 with a paired-comparison experiment of *edgeR* of the *R* package. Based on

602   FPKM value, the genes showing GFP^{Low}/GFP^{Neg}>2, GFP^{Low}-GFP^{Neg}>50 in GFP^{Low} microglia

603   and GFP^{High}/GFP^{Neg}>5, GFP^{High}-GFP^{Neg}>200 in GFP^{High} microglia were defined as upregulated

604   genes following MNs incorporation. The enrichment analyses were conducted using Enrichr

605   analysis tool (https://maayanlab.cloud/Enrichr/).

606

607   **Data availability**

608   The sequence data have been deposited in the DNA Data Bank of Japan (DDBJ) Sequence Read

609   Archive under the accession codes: DRA015927.

610

611   **Statistical analysis, image processing, and omics data analysis**

612   The statistical data were calculated by using GraphPad Prism (GraphPad Software) compared by

613   two-tailed Student's *t*-test and one-way ANOVA. Adobe Creative Could CC (Photoshop 22.1.0

614   and   Illustrator   25.0.1)   (https://www.adobe.com/),   FIJI   Image   J   2.1.0/1.53c

615   (https://imagej.nih.gov/ij/), and MATLAB (https://www.mathworks.com/) were used for all

616   image processing. The GO analysis obtained by proteomics screening was conducted by

617   Cytoscape v3.9.1.(https://cytoscape.org/) installed with Clue GO v2.5.9. plugin software.

618

References

1   Marquez-Ropero, M., Benito, E., Plaza-Zabala, A. & Sierra, A. Microglial Corpse Clearance: Lessons From Macrophages. *Front Immunol* **11**, 506, doi:10.3389/fimmu.2020.00506 (2020).

2   D'Mello, C., Le, T. & Swain, M. G. Cerebral microglia recruit monocytes into the brain in response to tumor necrosis factoralpha signaling during peripheral organ inflammation. *J Neurosci* **29**, 2089-2102, doi:10.1523/JNEUROSCI.3567-08.2009 (2009).

3   Chen, X. *et al.* Microglia-mediated T cell infiltration drives neurodegeneration in tauopathy. *Nature* **615**, 668-677, doi:10.1038/s41586-023-05788-0 (2023).

4   Li, Q. & Barres, B. A. Microglia and macrophages in brain homeostasis and disease. *Nat Rev Immunol* **18**, 225-242, doi:10.1038/nri.2017.125 (2018).

5   Wolf, S. A., Boddeke, H. W. & Kettenmann, H. Microglia in Physiology and Disease. *Annu Rev Physiol* **79**, 619-643, doi:10.1146/annurev-physiol-022516-034406 (2017).

6   Ueno, M. *et al.* Layer V cortical neurons require microglial support for survival during postnatal development. *Nat Neurosci* **16**, 543-551, doi:10.1038/nn.3358 (2013).

7   Cunningham, C. L., Martinez-Cerdeno, V. & Noctor, S. C. Microglia regulate the number of neural precursor cells in the developing cerebral cortex. *J Neurosci* **33**, 4216-4233, doi:10.1523/JNEUROSCI.3441-12.2013 (2013).

8   Aarum, J., Sandberg, K., Haeberlein, S. L. & Persson, M. A. Migration and differentiation of neural precursor cells can be directed by microglia. *Proc Natl Acad Sci U S A* **100**, 15983-15988, doi:10.1073/pnas.2237050100 (2003).

9   Miyamoto, A. *et al.* Microglia contact induces synapse formation in developing somatosensory cortex. *Nat Commun* **7**, 12540, doi:10.1038/ncomms12540 (2016).

10   Paolicelli, R. C. *et al.* Synaptic pruning by microglia is necessary for normal brain development. *Science* **333**, 1456-1458, doi:10.1126/science.1202529 (2011).

11   Schafer, D. P. *et al.* Microglia sculpt postnatal neural circuits in an activity and complement-dependent manner. *Neuron* **74**, 691-705, doi:10.1016/j.neuron.2012.03.026 (2012).

12   Badimon, A. *et al.* Negative feedback control of neuronal activity by microglia. *Nature* **586**, 417-423, doi:10.1038/s41586-020-2777-8 (2020).

650   13   Wake, H., Moorhouse, A. J., Miyamoto, A. & Nabekura, J. Microglia: actively surveying
651   and shaping neuronal circuit structure and function. *Trends Neurosci* **36**, 209-217,
652   doi:10.1016/j.tins.2012.11.007 (2013).

653   14   Prinz, M. & Priller, J. Microglia and brain macrophages in the molecular age: from origin
654   to neuropsychiatric disease. *Nat Rev Neurosci* **15**, 300-312, doi:10.1038/nrn3722 (2014).

655   15   Ginhoux, F. *et al.* Fate mapping analysis reveals that adult microglia derive from
656   primitive macrophages. *Science* **330**, 841-845, doi:10.1126/science.1194637 (2010).

657   16   Utz, S. G. *et al.* Early Fate Defines Microglia and Non-parenchymal Brain Macrophage
658   Development. *Cell* **181**, 557-573 e518, doi:10.1016/j.cell.2020.03.021 (2020).

659   17   Hattori, Y. *et al.* CD206(+) macrophages transventricularly infiltrate the early embryonic
660   cerebral wall to differentiate into microglia. *Cell Rep* **42**, 112092,
661   doi:10.1016/j.celrep.2023.112092 (2023).

662   18   Paolicelli, R. C. *et al.* Microglia states and nomenclature: A field at its crossroads.
663   *Neuron* **110**, 3458-3483, doi:10.1016/j.neuron.2022.10.020 (2022).

664   19   Kierdorf, K., Masuda, T., Jordao, M. J. C. & Prinz, M. Macrophages at CNS interfaces:
665   ontogeny and function in health and disease. *Nat Rev Neurosci* **20**, 547-562,
666   doi:10.1038/s41583-019-0201-x (2019).

667   20   Prinz, M., Masuda, T., Wheeler, M. A. & Quintana, F. J. Microglia and Central Nervous
668   System-Associated Macrophages-From Origin to Disease Modulation. *Annu Rev*
669   *Immunol* **39**, 251-277, doi:10.1146/annurev-immunol-093019-110159 (2021).

670   21   Nimmerjahn, A., Kirchhoff, F. & Helmchen, F. Resting microglial cells are highly
671   dynamic surveillants of brain parenchyma in vivo. *Science* **308**, 1314-1318,
672   doi:10.1126/science.1110647 (2005).

673   22   Haynes, S. E. *et al.* The P2Y12 receptor regulates microglial activation by extracellular
674   nucleotides. *Nat Neurosci* **9**, 1512-1519, doi:10.1038/nn1805 (2006).

675   23   Wake, H., Moorhouse, A. J., Jinno, S., Kohsaka, S. & Nabekura, J. Resting microglia
676   directly monitor the functional state of synapses in vivo and determine the fate of
677   ischemic terminals. *J Neurosci* **29**, 3974-3980, doi:10.1523/JNEUROSCI.4363-08.2009
678   (2009).

679   24   Mosher, K. I. *et al.* Neural progenitor cells regulate microglia functions and activity. *Nat*
680   *Neurosci* **15**, 1485-1487, doi:10.1038/nn.3233 (2012).

681   25   Pasciuto, E. *et al.* Microglia Require CD4 T Cells to Complete the Fetal-to-Adult
682   Transition. *Cell* **182**, 625-640 e624, doi:10.1016/j.cell.2020.06.026 (2020).

24

683   26   Crasta, K. *et al.* DNA breaks and chromosome pulverization from errors in mitosis.
684   *Nature* **482**, 53-58, doi:10.1038/nature10802 (2012).
685   27   Raab, M. *et al.* ESCRT III repairs nuclear envelope ruptures during cell migration to limit
686   DNA damage and cell death. *Science* **352**, 359-362, doi:10.1126/science.aad7611 (2016).
687   28   Denais, C. M. *et al.* Nuclear envelope rupture and repair during cancer cell migration.
688   *Science* **352**, 353-358, doi:10.1126/science.aad7297 (2016).
689   29   Fenech, M. *et al.* Micronuclei and disease - Report of HUMN project workshop at
690   Rennes 2019 EEMGS conference. *Mutat Res* **850-851**, 503133,
691   doi:10.1016/j.mrgentox.2020.503133 (2020).
692   30   Shi, L., Qalieh, A., Lam, M. M., Keil, J. M. & Kwan, K. Y. Robust elimination of
693   genome-damaged cells safeguards against brain somatic aneuploidy following Knl1
694   deletion. *Nat Commun* **10**, 2588, doi:10.1038/s41467-019-10411-w (2019).
695   31   Zhang, C. Z. *et al.* Chromothripsis from DNA damage in micronuclei. *Nature* **522**,
696   179-184, doi:10.1038/nature14493 (2015).
697   32   Papathanasiou, S. *et al.* Heritable transcriptional defects from aberrations of nuclear
698   architecture. *Nature* **619**, 184-192, doi:10.1038/s41586-023-06157-7 (2023).
699   33   Agustinus, A. S. *et al.* Epigenetic dysregulation from chromosomal transit in micronuclei.
700   *Nature* **619**, 176-183, doi:10.1038/s41586-023-06084-7 (2023).
701   34   Lin, Y. F. *et al.* Mitotic clustering of pulverized chromosomes from micronuclei. *Nature*
702   **618**, 1041-1048, doi:10.1038/s41586-023-05974-0 (2023).
703   35   Harding, S. M. *et al.* Mitotic progression following DNA damage enables pattern
704   recognition within micronuclei. *Nature* **548**, 466-470, doi:10.1038/nature23470 (2017).
705   36   Dou, Z. *et al.* Cytoplasmic chromatin triggers inflammation in senescence and cancer.
706   *Nature* **550**, 402-406, doi:10.1038/nature24050 (2017).
707   37   Mackenzie, K. J. *et al.* cGAS surveillance of micronuclei links genome instability to
708   innate immunity. *Nature* **548**, 461-465, doi:10.1038/nature23449 (2017).
709   38   Gluck, S. *et al.* Innate immune sensing of cytosolic chromatin fragments through cGAS
710   promotes senescence. *Nat Cell Biol* **19**, 1061-1070, doi:10.1038/ncb3586 (2017).
711   39   Yano, S. *et al.* A MATLAB-based program for three-dimensional quantitative analysis of
712   micronuclei reveals that neuroinflammation induces micronuclei formation in the brain.
713   *Sci Rep* **11**, 18360, doi:10.1038/s41598-021-97640-6 (2021).
714   40   Sekine, K., Honda, T., Kawauchi, T., Kubo, K. & Nakajima, K. The outermost region of
715   the developing cortical plate is crucial for both the switch of the radial migration mode

716   and the Dab1-dependent "inside-out" lamination in the neocortex. *J Neurosci* **31**,
717   9426-9439, doi:10.1523/JNEUROSCI.0650-11.2011 (2011).

718   41   Tabata, H. & Nakajima, K. Efficient in utero gene transfer system to the developing
719   mouse brain using electroporation: visualization of neuronal migration in the developing
720   cortex. *Neuroscience* **103**, 865-872, doi:10.1016/s0306-4522(01)00016-1 (2001).

721   42   Kubo, K. *et al.* Ectopic Reelin induces neuronal aggregation with a normal
722   birthdate-dependent "inside-out" alignment in the developing neocortex. *J Neurosci* **30**,
723   10953-10966, doi:10.1523/JNEUROSCI.0486-10.2010 (2010).

724   43   Mo, A. *et al.* Epigenomic Signatures of Neuronal Diversity in the Mammalian Brain.
725   *Neuron* **86**, 1369-1384, doi:10.1016/j.neuron.2015.05.018 (2015).

726   44   Frey, T. *et al.* Age-associated reduction of nuclear shape dynamics in excitatory neurons
727   of the visual cortex. *Aging Cell*, e13925, doi:10.1111/acel.13925 (2023).

728   45   Rello-Varona, S. *et al.* Autophagic removal of micronuclei. *Cell Cycle* **11**, 170-176,
729   doi:10.4161/cc.11.1.18564 (2012).

730   46   Komatsu, M. *et al.* Impairment of starvation-induced and constitutive autophagy in
731   Atg7-deficient mice. *J Cell Biol* **169**, 425-434, doi:10.1083/jcb.200412022 (2005).

732   47   Yamamoto, H., Zhang, S. & Mizushima, N. Autophagy genes in biology and disease. *Nat*
733   *Rev Genet* **24**, 382-400, doi:10.1038/s41576-022-00562-w (2023).

734   48   Ma, X. *et al.* CCT2 is an aggrephagy receptor for clearance of solid protein aggregates.
735   *Cell* **185**, 1325-1345 e1322, doi:10.1016/j.cell.2022.03.005 (2022).

736   49   Jung, S. *et al.* Analysis of fractalkine receptor CX(3)CR1 function by targeted deletion
737   and green fluorescent protein reporter gene insertion. *Mol Cell Biol* **20**, 4106-4114,
738   doi:10.1128/MCB.20.11.4106-4114.2000 (2000).

739   50   Abe, T. *et al.* Establishment of conditional reporter mouse lines at ROSA26 locus for live
740   cell imaging. *Genesis* **49**, 579-590, doi:10.1002/dvg.20753 (2011).

741   51   Ginhoux, F., Lim, S., Hoeffel, G., Low, D. & Huber, T. Origin and differentiation of
742   microglia. *Front Cell Neurosci* **7**, 45, doi:10.3389/fncel.2013.00045 (2013).

743   52   Bennett, M. L. *et al.* New tools for studying microglia in the mouse and human CNS.
744   *Proc Natl Acad Sci U S A* **113**, E1738-1746, doi:10.1073/pnas.1525528113 (2016).

745   53   Fritsch, L. E. *et al.* Type I Interferon Response Is Mediated by NLRX1-cGAS-STING
746   Signaling in Brain Injury. *Front Mol Neurosci* **15**, 852243,
747   doi:10.3389/fnmol.2022.852243 (2022).

748   54   Mason, C. E. *et al.* Standardizing the next generation of bioinformatics software
749   development with BioHDF (HDF5). *Adv Exp Med Biol* **680**, 693-700,
750   doi:10.1007/978-1-4419-5913-3_77 (2010).
751   55   McCarthy, D. J., Chen, Y. & Smyth, G. K. Differential expression analysis of multifactor
752   RNA-Seq experiments with respect to biological variation. *Nucleic Acids Res* **40**,
753   4288-4297, doi:10.1093/nar/gks042 (2012).
754   56   Li, Q. *et al.* Developmental Heterogeneity of Microglia and Brain Myeloid Cells
755   Revealed by Deep Single-Cell RNA Sequencing. *Neuron* **101**, 207-223 e210,
756   doi:10.1016/j.neuron.2018.12.006 (2019).
757   57   Zeisel, A. *et al.* Brain structure. Cell types in the mouse cortex and hippocampus revealed
758   by single-cell RNA-seq. *Science* **347**, 1138-1142, doi:10.1126/science.aaa1934 (2015).
759   58   Van Hove, H. *et al.* A single-cell atlas of mouse brain macrophages reveals unique
760   transcriptional identities shaped by ontogeny and tissue environment. *Nat Neurosci* **22**,
761   1021-1035, doi:10.1038/s41593-019-0393-4 (2019).
762   59   Krupina, K., Goginashvili, A. & Cleveland, D. W. Causes and consequences of
763   micronuclei. *Curr Opin Cell Biol* **70**, 91-99, doi:10.1016/j.ceb.2021.01.004 (2021).
764   60   Ginhoux, F. & Jung, S. Monocytes and macrophages: developmental pathways and tissue
765   homeostasis. *Nat Rev Immunol* **14**, 392-404, doi:10.1038/nri3671 (2014).
766   61   Drieu, A. *et al.* Parenchymal border macrophages regulate the flow dynamics of the
767   cerebrospinal fluid. *Nature* **611**, 585-593, doi:10.1038/s41586-022-05397-3 (2022).
768   62   Liu, C. *et al.* Macrophages Mediate the Repair of Brain Vascular Rupture through Direct
769   Physical Adhesion and Mechanical Traction. *Immunity* **44**, 1162-1176,
770   doi:10.1016/j.immuni.2016.03.008 (2016).
771   63   Masuda, T. *et al.* Specification of CNS macrophage subsets occurs postnatally in defined
772   niches. *Nature* **604**, 740-748, doi:10.1038/s41586-022-04596-2 (2022).
773   64   Ponpuak, M. *et al.* Secretory autophagy. *Curr Opin Cell Biol* **35**, 106-116,
774   doi:10.1016/j.ceb.2015.04.016 (2015).
775   65   Ejlerskov, P. *et al.* Tubulin polymerization-promoting protein (TPPP/p25alpha) promotes
776   unconventional secretion of alpha-synuclein through exophagy by impairing
777   autophagosome-lysosome fusion. *J Biol Chem* **288**, 17313-17335,
778   doi:10.1074/jbc.M112.401174 (2013).
779   66   Savina, A., Vidal, M. & Colombo, M. I. The exosome pathway in K562 cells is regulated
780   by Rab11. *J Cell Sci* **115**, 2505-2515, doi:10.1242/jcs.115.12.2505 (2002).

781 67   Hsu, C. *et al.* Regulation of exosome secretion by Rab35 and its GTPase-activating
782   proteins TBC1D10A-C. *J Cell Biol* **189**, 223-232, doi:10.1083/jcb.200911018 (2010).
783 68   Tsuboyama, K. *et al.* The ATG conjugation systems are important for degradation of the
784   inner autophagosomal membrane. *Science* **354**, 1036-1041, doi:10.1126/science.aaf6136
785   (2016).
786 69   Budnik, V., Ruiz-Canada, C. & Wendler, F. Extracellular vesicles round off
787   communication in the nervous system. *Nat Rev Neurosci* **17**, 160-172,
788   doi:10.1038/nrn.2015.29 (2016).
789 70   Christ, L., Raiborg, C., Wenzel, E. M., Campsteijn, C. & Stenmark, H. Cellular Functions
790   and Molecular Mechanisms of the ESCRT Membrane-Scission Machinery. *Trends*
791   *Biochem Sci* **42**, 42-56, doi:10.1016/j.tibs.2016.08.016 (2017).
792 71   Gong, Y. N. *et al.* ESCRT-III Acts Downstream of MLKL to Regulate Necroptotic Cell
793   Death and Its Consequences. *Cell* **169**, 286-300 e216, doi:10.1016/j.cell.2017.03.020
794   (2017).
795 72   Claude-Taupin, A. *et al.* ATG9A protects the plasma membrane from programmed and
796   incidental permeabilization. *Nat Cell Biol* **23**, 846-858, doi:10.1038/s41556-021-00706-w
797   (2021).
798 73   Hayakawa, K. *et al.* Transfer of mitochondria from astrocytes to neurons after stroke.
799   *Nature* **535**, 551-555, doi:10.1038/nature18928 (2016).
800 74   Joshi, A. U. *et al.* Fragmented mitochondria released from microglia trigger A1 astrocytic
801   response and propagate inflammatory neurodegeneration. *Nat Neurosci* **22**, 1635-1648,
802   doi:10.1038/s41593-019-0486-0 (2019).
803 75   Asai, H. *et al.* Depletion of microglia and inhibition of exosome synthesis halt tau
804   propagation. *Nat Neurosci* **18**, 1584-1593, doi:10.1038/nn.4132 (2015).
805 76   Yokoi, A. *et al.* Mechanisms of nuclear content loading to exosomes. *Sci Adv* **5**,
806   eaax8849, doi:10.1126/sciadv.aax8849 (2019).
807 77   Decout, A., Katz, J. D., Venkatraman, S. & Ablasser, A. The cGAS-STING pathway as a
808   therapeutic target in inflammatory diseases. *Nat Rev Immunol* **21**, 548-569,
809   doi:10.1038/s41577-021-00524-z (2021).
810 78   Paul, B. D., Snyder, S. H. & Bohr, V. A. Signaling by cGAS-STING in
811   Neurodegeneration, Neuroinflammation, and Aging. *Trends Neurosci* **44**, 83-96,
812   doi:10.1016/j.tins.2020.10.008 (2021).

813 79   Luteijn, R. D. *et al.* SLC19A1 transports immunoreactive cyclic dinucleotides. *Nature*
814   **573**, 434-438, doi:10.1038/s41586-019-1553-0 (2019).
815 80   Ritchie, C., Cordova, A. F., Hess, G. T., Bassik, M. C. & Li, L. SLC19A1 Is an Importer
816   of the Immunotransmitter cGAMP. *Mol Cell* **75**, 372-381 e375,
817   doi:10.1016/j.molcel.2019.05.006 (2019).
818 81   Carozza, J. A. *et al.* Extracellular cGAMP is a cancer cell-produced immunotransmitter
819   involved in radiation-induced anti-cancer immunity. *Nat Cancer* **1**, 184-196,
820   doi:10.1038/s43018-020-0028-4 (2020).
821 82   Hattori, Y. *et al.* Transient microglial absence assists postmigratory cortical neurons in
822   proper differentiation. *Nat Commun* **11**, 1631, doi:10.1038/s41467-020-15409-3 (2020).
823 83   Song, Y. *et al.* Transient nuclear deformation primes epigenetic state and promotes cell
824   reprogramming. *Nat Mater* **21**, 1191-1199, doi:10.1038/s41563-022-01312-3 (2022).
825 84   Moriyama, M., Koshiba, T. & Ichinohe, T. Influenza A virus M2 protein triggers
826   mitochondrial DNA-mediated antiviral immune responses. *Nat Commun* **10**, 4624,
827   doi:10.1038/s41467-019-12632-5 (2019).
828 85   Shinoda, T. *et al.* Elasticity-based boosting of neuroepithelial nucleokinesis via indirect
829   energy transfer from mother to daughter. *PLoS Biol* **16**, e2004426,
830   doi:10.1371/journal.pbio.2004426 (2018).
831 86   Goebbels, S. *et al.* Genetic targeting of principal neurons in neocortex and hippocampus
832   of NEX-Cre mice. *Genesis* **44**, 611-621, doi:10.1002/dvg.20256 (2006).
833 87   Okajima, T. *et al.* Atypical Cadherin FAT3 Is a Novel Mediator for Morphological
834   Changes of Microglia. *eNeuro* **7**, doi:10.1523/ENEURO.0056-20.2020 (2020).
835 88   Kim, J. *et al.* USP15 Deubiquitinates TUT1 Associated with RNA Metabolism and
836   Maintains Cerebellar Homeostasis. *Mol Cell Biol* **40**, doi:10.1128/MCB.00098-20
837   (2020).
838 89   Tsuruta, F., Okajima, T., Yano, S. & Chiba, T. Quantification of Endosome and
839   Lysosome Motilities in Cultured Neurons Using Fluorescent Probes. *J Vis Exp*,
840   doi:10.3791/55488 (2017).
841 90   Tabata, H. & Nakajima, K. Labeling embryonic mouse central nervous system cells by in
842   utero electroporation. *Dev Growth Differ* **50**, 507-511,
843   doi:10.1111/j.1440-169X.2008.01043.x (2008).

844   91   Morrison, H., Young, K., Qureshi, M., Rowe, R. K. & Lifshitz, J. Quantitative microglia
845   analyses reveal diverse morphologic responses in the rat cortex after diffuse brain injury.
846   *Sci Rep* **7**, 13211, doi:10.1038/s41598-017-13581-z (2017).

847   92   Fenech, M. *et al.* HUMN project: detailed description of the scoring criteria for the
848   cytokinesis-block micronucleus assay using isolated human lymphocyte cultures. *Mutat*
849   *Res* **534**, 65-75, doi:10.1016/s1383-5718(02)00249-8 (2003).

850   93   Mure, K., Takeshita, T. & Morimoto, K. Categorization of micronuclei by size and
851   measurement of each ratio in cytokinesis-block and conventional cultures of human
852   lymphocytes exposed to mitomycin C and colchicine. *Environ Health Prev Med* **1**, 93-99,
853   doi:10.1007/BF02931197 (1996).

854   94   Kishi, Y. & Gotoh, Y. Isolation of genetically manipulated neural progenitors and
855   immature neurons from embryonic mouse neocortex by FACS. *STAR Protoc* **2**, 100540,
856   doi:10.1016/j.xpro.2021.100540 (2021).

857

858   **Figure legends**

859

860   **Fig. 1 Neuronal micronuclei are generated from migrating neurons**

861   (a) Staining of nuclei in the cerebral cortex of embryonic mice (E18.5). The yellow arrow

862   indicates the micronucleus. Scale bar: 10 μm. (b) MNs mostly exist in the MZ and CP (PCZ) but

863   not CP (w/o PCZ). Scale bar: 100 μm (left), 20 μm (right), E18.5 (c) The graph shows the

864   population of MNs in each field. 12 fields obtained from 2 brains, 2.56 x 10^4 μm^2/field; mean ±

865   SEM, *p* values were analyzed by one-way analysis of variance (ANOVA) Tukey's multiple

866   comparisons test. (d) The transmission electron microscopy (TEM) images of the cerebral cortex

867   of ICR mice. E18.5. N; Nucleus, MN; Micronucleus, Scale bars: 20 μm. (e) Immunostaining of

868   migrating neurons in the cerebral cortex. EGFP plasmids were introduced using *in utero*

869   electroporation at E14.5. The GFP$^+$ neurons were detected at E18.5. MN exists in the neuronal

870   process in the vicinity of the brain surface. Yellow arrows indicate MNs. Scale bar: 20 μm. (f)

871   Immunostaining of migrating neurons in the aggregated area. Reelin plasmids were introduced

872   using *in utero* electroporation at E14.5. Scale bar: 20 μm. Yellow arrows indicate micronucleus.

873   The GFP$^+$ neurons were detected at E18.5. MNs exist in the processes in the center of neuronal

874   aggregation. (g) Immunostaining of GFP$^+$ small nuclei in the cerebral cortex of

875   *NexCre:LSL-Sun1GFP* mice. P0 (left), P7 (center), and P14 (right). Scale bar: 20 μm (P0 and

876   P7) and 50 μm (P14). A dotted line indicates the pial surface. (h) The graph shows the

877   percentage of GFP$^+$-MNs in the cerebral cortex. n=4 mice, mean ± SEM, *p* value was analyzed

878   by Mann-Whitney test. (i) Immunostaining of *NexCre:LSL-Sun1GFP* mice brain. The

879   high-magnification images obtained from the cerebral cortex of *NexCre:LSL-Sun1GFP* mice

880   were integrated into a tiling image (center). The typical MNs in Layer 1 are shown in the right

881   panel. P14. Scale bar: 20 μm. (j) The data shows the frequency of micronuclear appearance in

882   Layer 1 of the cerebral cortex. The vertical axis represents the relative value when the maximum

883   number of MNs is defined as 100. The data was quantified using MATLAB software, CAMDi[39].

884

885   **Fig. 2 Neuronal micronuclei are propagated to microglia**

886   (a) Schematic illustration of micronuclear transfer from neuron to microglia. (b) Staining of

887   micronucleus in primary cultured neurons (5 DIV). Scale bar: 20 μm. (c) Immunostaining of

888   GFP$^+$ small nuclei in the extracellular space (MAP2$^-$, S100β$^-$) of cerebral cortex. P14. Scale bar:

889   10 μm. (d) TEM images of the cerebral cortex of ICR mice. E18.5. MN; Micronucleus, Cyto;

890   Cytoplasmic space, Scale bars: 20 μm (left) and 1.0 μm (right). (e) Schematic illustration for

31

891 fractionation of extracellular MNs. P0.4: apoptotic cells fraction, P2: nuclear fraction, P15:

892 micronuclear fraction, P120: exosome fraction. (f) Immunoblotting of the extracellular MNs

893 obtained from primary cultured cortical neurons of *NexCre:LSL-Sun1GFP* mice. (g) Pie chart

894 showing the composition of the extracellular MNs by gene ontology (GO) analysis. (h) The GO

895 mapping and functional annotation of extracellular MNs components. (i) Immunostaining of

896 GFP$^+$-MNs in the Iba1$^+$ microglia in Layer 1. *NexCre:LSL-Sun1GFP* mice, P14. Scale bar: 50

897 μm. White arrowheads indicate MNs in microglia. Yellow arrows indicate extracellular MNs. (j)

898 Image is the inset of Fig. 2i. Neuronal micronucleus is taken in the microglia. MIP: maximum

899 intensity projection image, interval: 1 μm per image, 11 Z-stack images.

900

901 **Fig. 3 Micronuclei affect microglial morphology during the early-postnatal period via**

902 **cGAS**

903 (a) Schematic illustration of microglial complexity. (b) Immunostaining of Iba1$^+$ microglia with

904 or without neuronal MNs. White arrowheads indicate GFP$^-$ micronucleus (GFP$^-$-MN). Yellow

905 arrows indicate GFP$^+$ micronucleus (GFP$^+$-MN). Scale bar: 50 μm. (c) The graph shows the

906 process length in the presence or absence of MNs. 4 brains. mean ± SEM, *p* values were

907 analyzed by one-way ANOVA Dunnett's multiple comparisons test. (d) The graph shows the

908 number of processes in the presence or absence of MNs. 4 brains. mean ± SEM, *p* values were

909 analyzed by one-way ANOVA Dunnett's multiple comparisons test. (e) Immunostaining of Iba1$^+$

910 microglia in the cerebral cortex of either WT or *cGAS$^{-/-}$* mice. P6. MN$^-$ microglia (left) and MN$^+$

911 microglia (right). Yellow arrows indicate MNs. Scale bar: 10 μm. (f)(g) The graphs show the

912 analyses of microglial morphology. 2 brains. (f) the number of processes, (g) process length,

913 mean ± SEM, *p* values were analyzed by one-way ANOVA Tukey's multiple comparisons test.

914 (h) Immunostaining of Iba1$^+$ microglia in the cerebral cortex of either WT or *cGAS$^{-/-}$* mice. P14.

915 MN$^-$ microglia (left) and MN$^+$ microglia (right). Yellow arrows indicate MNs. Scale bar: 10 μm.

916 (i)(j) The graphs show the analyses of microglial morphology. 2 brains. (i) the number of

917 processes, (j) process length, mean ± SEM, *p* values were analyzed by one-way ANOVA

918 Tukey's multiple comparisons test.

919

920 **Fig. 4 Neural micronuclei alter a hallmark of microglia**

921 (a) The *NexCre:LSL-Sun1GFP* mice brains were homogenized using Dounce tissue homogenizer.

922 Myelinated materials were removed using Percoll gradient. Microglia were purified by FACS

923 using anti-CD11b antibody and GFP signals, followed by conducting bulk-RNA seq analysis. (b)

924 Representative gating strategy for flow cytometry of either GFP$^+$ or GFP$^-$ microglia from the
925 *NexCre:LSL-Sun1GFP* whole brain (P8, P9, P10). (left) Non-microglial population, (right)
926 Microglial population, left gate; GFP^{Neg} microglia, center gate; GFP^{Low} microglia, right gate;
927 GFP^{High} microglia. (c) The simplified diagram for the deferential gene expression (DEG)
928 analysis. The number of DEG in each microglial population categorized by GFP intensity
929 (GFP^{Neg}, GFP^{Low}, GFP^{High}). (d) The GO enrichment analysis of DEG in GFP^{Low} MN$^+$ microglia
930 (591 genes). Data was analyzed in Enrichr analysis tool. (e) The scatter plot indicates the ratio
931 and differences of FPKM between GFP^{Neg} MN$^-$ microglia and GFP^{Low} MN$^+$ microglia. FPKM:
932 GFP^{Low}/GFP^{Neg}>2, GFP^{Low}-GFP^{Neg}>50. (f) The Heat map indicates the comparison of FPKM
933 among GFP^{Neg} MN$^-$ microglia, GFP^{Low} MN$^+$ microglia, and GFP^{High} MN$^+$ microglia. FPKM:
934 GFP^{Low}/GFP^{Neg}>2, GFP^{Low}-GFP^{Neg}>50. (g) Immunostaining of Iba1$^+$ microglia with or without
935 neuronal MNs. White arrowheads indicate GFP$^-$ micronucleus (GFP$^-$-MN). Yellow arrows
936 indicate GFP$^+$ micronucleus (GFP$^+$-MN). Scale bar: 50 μm. (h) The graph shows the
937 fluorescence intensity of CD206 in the presence or absence of MNs. More than 13 images
938 obtained from two independent *NexCre:LSL-Sun1GFP* brain, P7; mean ± SEM, *p* values were
939 analyzed by one-way ANOVA Dunnett's multiple comparisons test. (i) Immunostaining of Iba1$^+$
940 microglia with neuronal MNs in the meninges. Yellow arrows indicate GFP$^+$MN. (j) Schematic
941 model for regulating microglial state by neuronal MNs.

942

943 **Acknowledgments**

944

955

956 **Author contributions**

957

958 S.Y. and F.T. designed research; S.Y., N.A., Y.K., H.K., K.A., A.K., K.H., K.K., T.O., B.S., and

959 F.T. performed research; S.Y., N.A., Y.K., H.K., K.A., A.K., M.S.,T.N. and F.T. analyzed data;

960 T.N developed MATLAB program; Y.K., Y.G., and I.T. provide materials. S.Y and F.T. wrote

961 the paper. Study supervision: Y.G., K.N., T.C. and F.T

962

Extended Data Fig. 1

(a) Immunostaining of MAP2$^+$ neurons. Primary cultured neurons (5 DIV) were stimulated with the recombinant 100 ng/ml Reelin for 6 hours. Scale bar: 10 μm. (b) The graph shows the percentage of MN$^+$ neurons. 10 fields, n=3 independent samples, mean ± SEM, p value was calculated by Student's t-test. (c) Schematic illustration for injecting recombinant Reelin. (d) The recombinant Reelin (100 ng) was stimulated into the mice brain for 6 hours, and the brain sections were stained using DAPI . P7, Scale bar: 20 μm. (e) The graph shows the percentage of MNs. 15 images obtained from three independent brain, mean ± SEM, p value was calculated by Student's t-test. (f) Schematic illustration for an *in vitro* migration assay. (g) Immunostaining of migrated neurons at the bottom sides of the trans-well. Nuclear shapes were detected by Lamin B1 staining. Asterisks indicate the marks of the hole. Arrow indicates the micronucleus. Scale bar: 10 μm. Illustration indicates the condition of migration, herniation, and micronuclear formation. (h) Immunostaining of migrated neurons at the bottom side of the trans-well. Yellow arrows indicate MNs. Scale bar: 10 μm. (i)(j) The graph shows the population of MN$^+$ neurons.(i) n=6, (j) n=3 trans-wells. More than 200 neurons were analyzed from one trans-well. (i) pore size; 3 μm, (j) pore size 12 μm, mean ± SEM, p value was calculated by Student's t-test. (k) Schematic illustration for an *in vitro* mechanical stress assay. Neuro2A cells received mechanical stresses by pumping. (l) Neuro2A cells were stained with Hoechst. MNs were generated by mechanical stress. Scale bar: 10 μm (m) The graph shows the percentage of population of MN$^+$ cells. Low; 5.0 x 10^4 cells/300μl, High; 5.0 x 10^4 cells/150μl, n=9 images, mean ± SEM, p values were calculated by one-way ANOVA Dunnett's multiple comparison test.

Extended Data Fig. 2

(a) Immunostaining of MAP2$^+$ neurons in the cerebral cortex of either WT or *NexCre:Atg7$^{f/f}$* at P21. Yellow arrows indicate MNs. Scale bar: 20 μm. (b) The graph shows the population of MNs in the cerebral cortex. n=20 images, 10 images obtained from two independent brain; mean ± SEM, p value was calculated by Student's t-test. (c) Immunostaining of Iba1$^+$ microglia in the cerebral cortex of either WT or *NexCre:Atg7$^{f/f}$* at P21. Yellow arrows indicate MNs. Scale bar: 20 μm. (d) The graph shows the percentage of MNs$^+$ microglia in the cerebral cortex. Data were combined from 3 independent brains (8 images per brain, total 24 images), mean ± SEM, p value was calculated by Student's t-test. (e) Immunoblotting of the extracellular MNs (P15) obtained from primary cortical neurons in the presence or absence of 100 nM BafA treatment. (f) Primary cortical neurons were stimulated with either 300 nM BafA for 3 hours or 50 μM etoposide (Eto,

35

996 positive control for inducing apoptosis) for 24 hours. Immunostaining of cleaved-caspase 3 and

997 MAP2$^+$ cortical neurons (5 DIV). Scale bar: 50 μm. (g) The graph shows the fluorescence

998 intensity of cleaved-caspase 3 with MAP2. mean ± SEM, p values were calculated by one-way

999 ANOVA Dunnett's multiple comparison test. (h) Schematic illustration of the collection of

1000 extracellular micronuclear for immunocytochemistry. (i) Immunostaining of Tubulin and Rab35

1001 resided in the extracellular MNs. Scale bar: 20 μm. (j) Immunostaining of transfected TCP

1002 subunits in the migrated neurons at the bottom side of the trans-well (3 DIV). Yellow arrows

1003 indicate MNs. Scale bar: 10 μm. (k) Immunostaining of GFP$^+$-MNs in the cerebral cortex. A

1004 small amount of Tubulin resided in GFP$^+$-MNs. P14. Scale bar: 10 μm. (l) Immunostaining of

1005 GFP$^+$ MNs in the cerebral cortex. MAP2 and LC3 resided in GFP$^+$-MNs. P14. Scale bar: 20 μm

1006 (upper) and 5 μm (bottom). (m) Working hypothesis of micronuclear secretion dependent on

1007 autophagy-lysosome machinery. TCP subunit is a potential receptor linking the micronucleus to

1008 LC3.

1009

1010 **Extended Data Fig. 3**

1011 (a) Schematic illustration for an *in vitro* micronuclear transfer assay. (b) TEM image of BV2

1012 cells after treatment with conditioned medium. NE: nuclear envelope, MN: micronucleus, Cyto:

1013 cytoplasm. Scale bar: 1.0 μm. (c) Immunostaining of BV2 cells with GFP$^-$-and GFP$^+$-MNs. Scale

1014 bar: 20 μm. (d) Immunostaining of GFP$^-$- and GFP$^+$-MNs in BV2. Yellow arrow indicates

1015 micronucleus. Scale bar: 10 μm. (e) The graph shows the percentage of neuronal MNs (GFP$^+$

1016 MNs) containing BV2 cells after treatment with a conditioned medium. Each spot indicates the

1017 combined value of 10 images from one experiment. n=3 independent experiments. NB; fresh

1018 neurobasal medium, mean ± SEM, p values were analyzed by one-way ANOVA Dunnett's

1019 multiple comparisons test. (f) Schematic illustration for eliminating MNs. (g) The graph shows

1020 MNs$^+$ BV2 cells after treatment with a conditioned medium. mean ± SEM, p value was

1021 calculated by one-way ANOVA Tukey's multiple comparisons tests. Each spot indicates the

1022 combined value of more than 9 images from one experiment. Each column indicates a set of 3

1023 independent experiments. (h) Live imaging of *Cx3cr1-EGFP*;*H2B-mCherry* cortical slice culture

1024 (P3). The interval of taking images was every 5 min. Yellow arrowheads indicate MN in the

1025 microglia. Cyan asterisks indicate MN out of the microglia. No.1-6, 89 z-stack images/field, No.

1026 7-24, 92 z-stack images/field, 1.5 μm pitch. Scale bar: 10 μm.

1027

1028 **Extended Data Fig. 4**

36

1029   (a) Tailing immunostained images of Iba1$^+$ microglia in the cerebral cortex. WT, P14. Scale bar:

1030   20 μm. (b) Representative images of microglia in Layer 1 (L1) and Layers 2-6 (L2-6) from the

1031   insets of Extended Data Fig. 4a. Scale bar: 20 μm. (c)(d) The graphs show the analyses of

1032   microglial characters. 3 brains. (c) Process length, (d) the number of the process. mean ± SEM, p

1033   value was calculated by Student's t-test.

1034

1035   **Extended Data Fig. 5**

1036   (a) Immunostaining of Iba1$^+$ and CD68$^+$ microglia with or without MNs (MN$^-$;

1037   micronuclei-negative, MN$^+$; micronuclei-positive). P14, Scale bar: 10 μm. (b) The graph shows

1038   the expression level of CD68. The numbers counted are shown in the graph. 5 brains. mean ±

1039   SEM, p values were analyzed by one-way ANOVA Dunnett's multiple comparisons test.   (c)

1040   Immunostaining of Iba1$^+$ and Tmem119$^+$ microglia with or without MNs. P14, Scale bar: 10 μm.

1041   (d) The graph shows the expression level of Tmem119. The numbers counted are shown in the

1042   graph. 3 brains. mean ± SEM, p values were analyzed by one-way ANOVA Dunnett's multiple

1043   comparisons test. (e) Immunostaining of Iba1$^+$ and P2ry12$^+$ microglia with or without MNs. The

1044   numbers counted are shown in the graph. P14, Scale bar: 10 μm. (f) The graph shows the

1045   expression level of P2ry12. 5 brains, mean ± SEM, p values were analyzed by one-way ANOVA

1046   Dunnett's multiple comparisons test.

1047

1048   **Extended Data Fig. 6**

1049   (a) The graph shows the expression level of cGAS mRNA in each cell (ASC; astrocyte, NEUR;

1050   neuron, OPC; oligodendrocyte precursor cell, iOLG; immature oligodendrocyte, mOLG;

1051   myelinating oligodendrocyte, MG/MAC; microglia/macrophage, EC; Endothelial cell). This data

1052   was obtained from the Brain RNA-Seq database (https://www.brainrnaseq.org/). (b)

1053   Immunostaining of Iba1$^+$ microglia in the cerebral cortex of either WT or *cGAS$^{-/-}$* mice at P6.

1054   Scale bar: 20 μm. (c)-(e) The graphs show the analyses of microglial state. 2 brains. The numbers

1055   in the graph represent the numbers of cells counted. (c) The number of processes, (d) process

1056   length, (e) expression level of CD68. mean ± SEM, p values were analyzed by Student's t-test. (f)

1057   Immunostaining of CD68 in Iba1$^+$ microglia of either WT or *cGAS$^{-/-}$* mice, P6, Scale bar: 10 μm.

1058   (g) The graph show the expression level of CD68. The numbers in the graph represent the

1059   numbers of cells counted. mean ± SEM, 2 brains. p values were analyzed by one-way ANOVA

1060   Tukey's multiple comparisons test. (h) Immunostaining of CD68 in Iba1$^+$ microglia of either WT

1061   or *cGAS$^{-/-}$* mice, MN$^-$; micronuclei-negative, MN$^+$; micronuclei-positive. P14, Scale bar: 10 μm.

37

1062 (i) The graph show the expression level of CD68. The numbers in the graph represent the

1063 numbers of cells counted. mean ± SEM, 2 brains. *p* values were analyzed by one-way ANOVA

1064 Tukey's multiple comparisons test.

1065

1066 **Extended Data Fig. 7**

1067 (a) Representative gating strategy for microglia in *NexCre:LSL-Sun1GFP* mice. (b) The GO

1068 enrichment analysis of DEG in GFP^{High} MN$^+$ microglia (1,663 genes). Data was analyzed by

1069 Enrichr analysis tool. (c) The scatter plot indicates the ratio and differences of FPKM between

1070 GFP^{Neg} MN$^-$ microglia and GFP^{High} MN$^+$ microglia. FPKM: GFP^{High}/GFP^{Neg}>5,

1071 GFP^{High}-GFP^{Neg}>200, (d) The Heat map indicates the comparison of FPKM among GFP^{Neg} MN$^-$

1072 microglia, GFP^{Low} MN$^+$ microglia, and GFP^{High} MN$^+$ microglia.. FPKM: GFP^{High}/GFP^{Neg}>5,

1073 GFP^{HIgh}-GFP^{Neg}>200 (e)-(r) The graph shows the expression of each gene obtained from

1074 bulk-RNAseq analysis in GFP^{High} MN$^+$ microglia. (ASC; astrocyte, NEUR; neuron, OPC;

1075 oligodendrocyte precursor cell, iOLG; immature oligodendrocyte, mOLG; myelinating

1076 oligodendrocyte, MG/MAC; microglia/macrophage, EC; Endothelial cell). This data was

1077 obtained from the Brain RNA-Seq database (https://www.brainrnaseq.org/).

1078

1079 **Extended Data Fig. 8**

1080 (a)-(k) The graphs show the value of FPKM obtained from bulk-RNAseq analysis in GFP^{Low}

1081 MN$^+$ microglia. Top 11 genes out of 591 genes are represented, FPKM: GFP^{Low}/ GFP^{Neg}>2,

1082 GFP^{Low}-GFP^{Neg}>50. (l)-(v) The graph shows the expression of each gene obtained from

1083 bulk-RNAseq analysis in GFP^{High} MN$^+$ microglia. (ASC; astrocyte, NEUR; neuron, OPC;

1084 oligodendrocyte precursor cell, iOLG; immature oligodendrocyte, mOLG; myelinating

1085 oligodendrocyte, MG/MAC; microglia/macrophage, EC; Endothelial cell). This data was

1086 obtained from the Brain RNA-Seq database (https://www.brainrnaseq.org/).
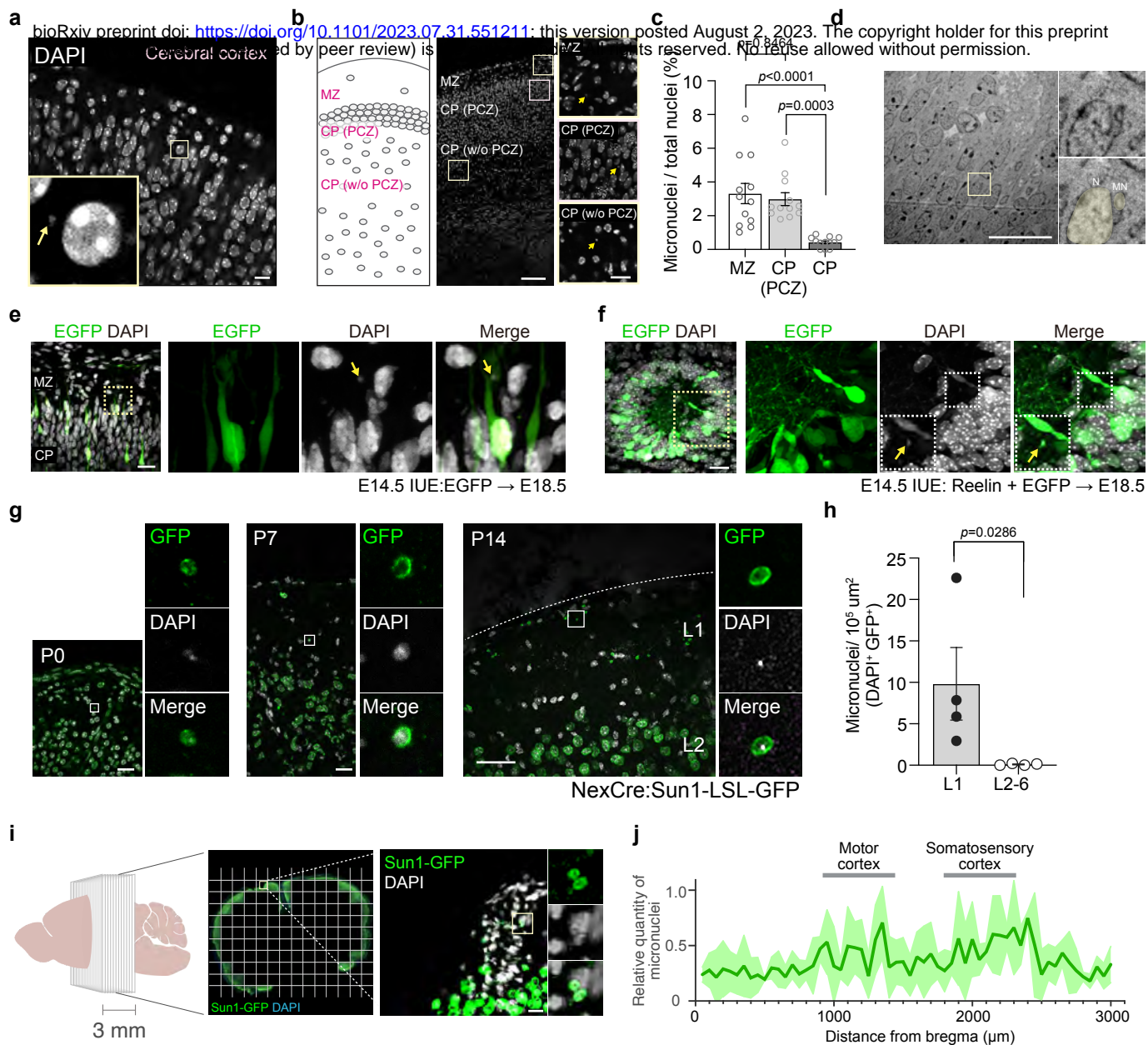
1087

1088

1089

Fig. 1
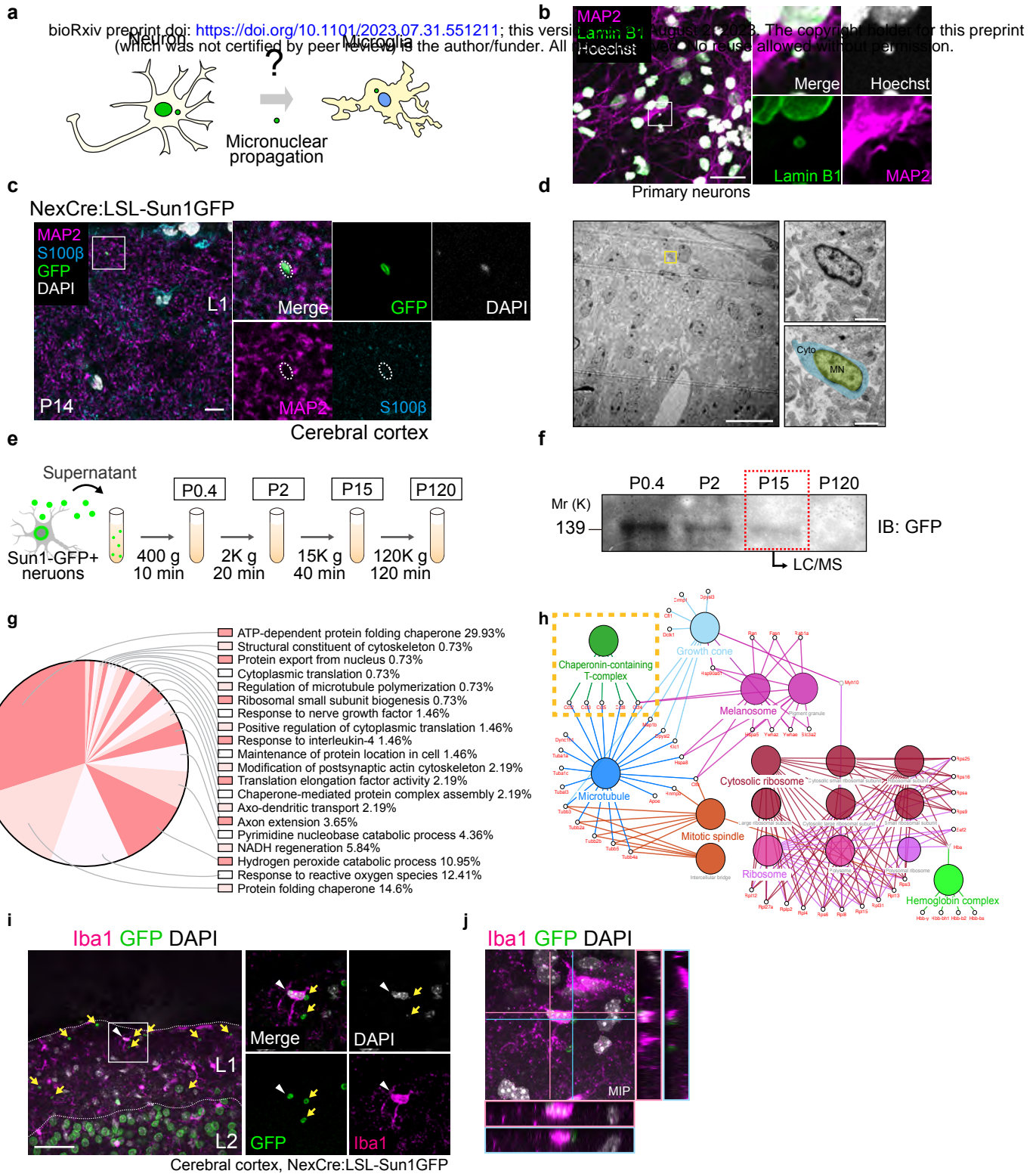**Neuronal micronuclei are generated from migrating neurons**

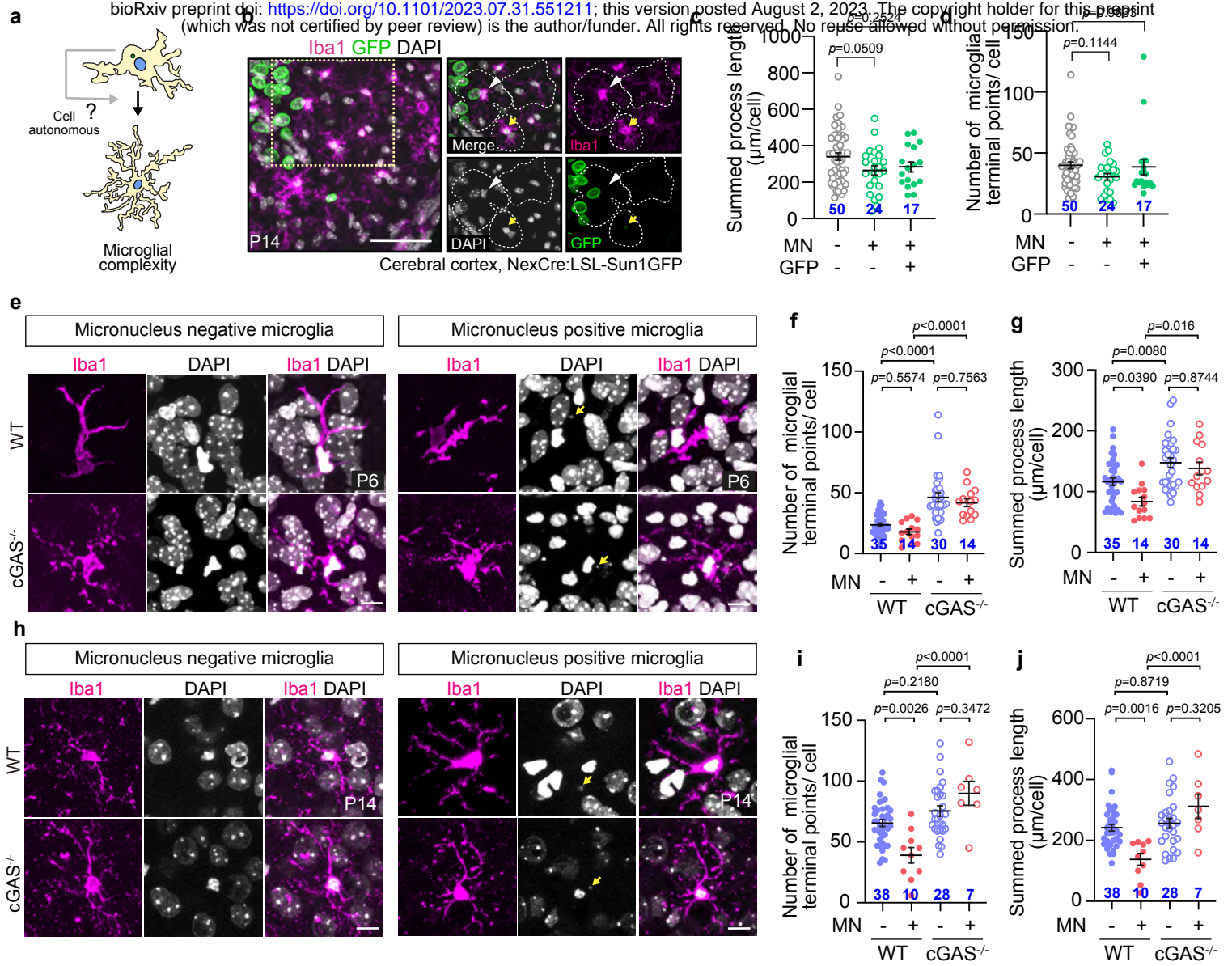**Fig. 2**
Neuronal micronuclei are propagated to microglia

Fig. 3
Micronuclei affect microglial morphology during the early-postnatal period via cGAS

a

SUN1-GFP mice brain

Percall gradient

FACS sorting
CD11b Ab
GFP

RNAseq

b

c

Total number of detected genes; **54,752 genes**
Sum of the three groups; **2,571 genes**

MN⁻ microglia
317 genes
$GFP^{Neg} > GFP^{Low}$
and
$GFP^{Neg} > GFP^{High}$

MN+ microglia (Type 1)
591 genes
$GFP^{Neg} < GFP^{Low} > GFP^{High}$

MN+ microglia (Type 2)
1,663 genes
$GFP^{Neg} < GFP^{High}$
and
$GFP^{Low} < GFP^{High}$

d

The genes identified in GFP^{Low} microglia (591 genes)

Collagen-containing extracellular matrix (GO:0062023)
Basement membrane (GO:0005604)
Cell-substrate junction (GO:0030055)
Bleb (GO:0032059)
Focal adhesion (GO:0005925)
Basolateral plasma membrane (GO:0016323)
Cell-cell junction (GO:0005911)
Early phagosome (GO:0032009)
Endoplasmic reticulum lumen (GO:0005788)
Coated vesicle (GO:0030135)

GO_Cellular_Component_2021

e

591 genes

CD206
Dab2
Stab1
Slc40a1

Col1a2
Col1a1
Col3a1

Low/Neg>2
Low-Neg>50

Genes in GFP^{Low} MG
Genes in GFP^{Neg} MG

BAMs
ECM

f

	GFP^Neg (MN⁻ MG)	GFP^Low (MN⁺ MG)	GFP^High (MN⁺ MG)
	123456789	123456789	123456789

Gm10925
CD206
Dab2
Gm29216
Stab1
Col1a2
Col1a1
Gm28661
Col3a1
Gm28438
Slc40a1
Apbb1ip
Cxcl12
Gm13340
Ctsc
Enpp1

0 — 3.0x10³

g

CD206	Hoechst	GFP	Iba1	CD206 Iba1 Hoechst GFP

MN⁻

MN⁺

MN⁺ GFP⁺

P14

h

p=0.0417
p=0.001

CD206 intensity (A.U.)

8

60   15   14

| MN | - | + | + |
| GFP | - | - | + |

i

Iba1 CD206 GFP DAPI

MIP

Merge | Hoechst | GFP
CD206 | Iba1

CD206 GFP DAPI

j

L1
L2

?

ECM-related proteins
ECM

MNs⁺ microglia

Immune response
Phgocytosis
Synaptic connectivity

MNs⁻ microglia

MNs
↓
cGAS
∞ cGAMP
STING
IRF3
NFκB

Regulating microglial signatures

Microglial diversity

ECM-related proteins
Col1a1, Col1a2, Col3a1, etc
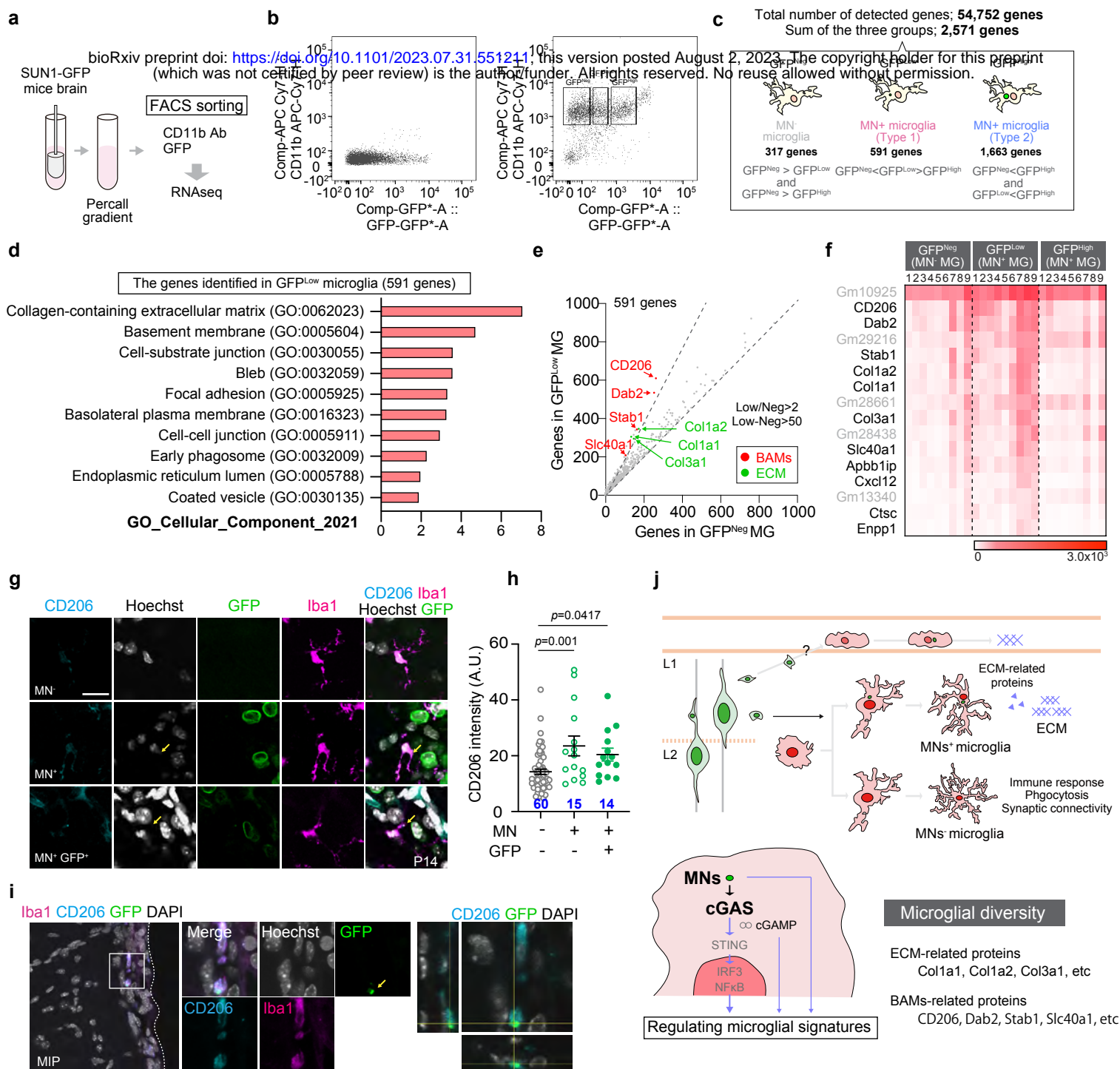
BAMs-related proteins
CD206, Dab2, Stab1, Slc40a1, etc

Fig. 4
Neuronal micronuclei alter a hallmark of microglia